J Appl Physiol 127: 1386–1402, 2019.
First published August 1, 2019; doi:10.1152/japplphysiol.00015.2019.

RESEARCH ARTICLE

A model-based analysis of autonomic nervous function in response to the Valsalva maneuver

E. Benjamin Randall,[1] Anna Billeschou,[2] Louise S. Brinth,[2] Jesper Mehlsen,[3] and Mette S. Olufsen[1]

[1]*Department of Mathematics, North Carolina State University, Raleigh, North Carolina;* [2]*Department of Clinical Physiology and Nuclear Medicine, Bispebjerg Frederiksberg Hospital, Frederiksberg, Denmark; and* [3]*Section of Surgical Pathophysiology, Juliane Marie Centre, Rigshospitalet, Copenhagen University Hospital, Copenhagen, Denmark*

Submitted 11 January 2019; accepted in final form 22 July 2019

Randall EB, Billeschou A, Brinth LS, Mehlsen J, Olufsen MS. A model-based analysis of autonomic nervous function in response to the Valsalva maneuver. *J Appl Physiol* 127: 1386–1402, 2019. First published August 1, 2019; doi:10.1152/japplphysiol.00015.2019.—The Valsalva maneuver (VM) is a diagnostic protocol examining sympathetic and parasympathetic activity in patients with autonomic dysfunction (AD) impacting cardiovascular control. Because direct measurement of these signals is costly and invasive, AD is typically assessed indirectly by analyzing heart rate and blood pressure response patterns. This study introduces a mathematical model that can predict sympathetic and parasympathetic dynamics. Our model-based analysis includes two control mechanisms: respiratory sinus arrhythmia (RSA) and the baroreceptor reflex (baroreflex). The RSA submodel integrates an electrocardiogram-derived respiratory signal with intrathoracic pressure, and the baroreflex submodel differentiates aortic and carotid baroreceptor regions. Patient-specific afferent and efferent signals are determined for 34 control subjects and 5 AD patients, estimating parameters fitting the model output to heart rate data. Results show that inclusion of RSA and distinguishing aortic/carotid regions are necessary to model the heart rate response to the VM. Comparing control subjects to patients shows that RSA and baroreflex responses are significantly diminished. This study compares estimated parameter values from the model-based predictions to indices used in clinical practice. Three indices are computed to determine adrenergic function from the slope of the systolic blood pressure in phase II [α (a new index)], the baroreceptor sensitivity (β), and the Valsalva ratio (γ). Results show that these indices can distinguish between normal and abnormal states, but model-based analysis is needed to differentiate pathological signals. In summary, the model simulates various VM responses and, by combining indices and model predictions, we study the pathologies for 5 AD patients.

NEW & NOTEWORTHY We introduce a patient-specific model analyzing heart rate and blood pressure during a Valsalva maneuver (VM). The model predicts autonomic function incorporating the baroreflex and respiratory sinus arrhythmia (RSA) control mechanisms. We introduce a novel index (α) characterizing sympathetic activity, which can distinguish control and abnormal patients. However, we assert that modeling and parameter estimation are necessary to explain pathologies. Finally, we show that aortic baroreceptors contribute significantly to the VM and RSA affects early VM.

baroreflex mechanism; carotid and aortic baroreceptors; mathematical modeling; parameter estimation; sympathetic and parasympathetic activity

INTRODUCTION

Patients with autonomic nervous system dysfunction (AD) affecting the cardiovascular control system exhibit a wide array of symptoms, including dizziness, syncope, and widespread pain, which complicate intervention protocols and potentially lead to incorrect diagnoses (43). Given the complex interaction of stimuli arising from multiple centers, understanding the mechanisms that cause AD is challenging. Autonomic function is commonly studied indirectly by observing changes in blood pressure and heart rate in a controlled setting in response to postural or respiratory challenges or drug intervention (1, 8, 19, 28, 34, 62, 76). The objective of our study is to build a mathematical model that can analyze autonomic function for subjects undergoing a Valsalva maneuver (VM), a clinical test used to assess the autonomic ability to compensate for acute changes in central blood volume and pressure (34, 65).

In this study, we focus on the VM, which activates both parasympathetic and sympathetic branches of the autonomic nervous system in sitting patients, inducing short-term changes in autonomic activity (34, 57). This study develops a new mechanistic mathematical model providing a hypothesis for interactions of both the afferent and efferent neural pathways. Mathematical modeling used in this study and by others (10, 30, 38, 40) is advantageous, as it enables us to analyze explicitly the effect of hypothesized pathways and predict responses to interventions by changing parameters or pathways in the model. Another common method for analyzing physiological signals is using signal processing methods (5, 67), which are excellent for determining changes in frequency-based responses but unable to describe signal transmission via specific pathways or predict responses to interventions.

Several deterministic mathematical models have been proposed to explain the autonomic response to the VM. These can be split into the following two categories: *1*) closed-loop models simulating blood pressure and heart rate dynamics simultaneously (30, 37, 40, 59) and *2*) open-loop models that either take blood pressure as an input and compute heart rate as an output or take heart rate as an input and compute blood pressure as an output (10, 35). In this study, we pursue the open-loop approach, predicting changes in heart rate in response to the VM. Our model distinguishes between the baroreceptor reflex (baroreflex) and respiratory sinus arrhythmia (RSA) control mechanisms. Others have modeled the interaction between the respiratory and cardiovascular systems (3, 12, 39, 40). However, these studies have respiratory models

Address for reprint requests and other correspondence: M. Olufsen, SAS Hall 3216, Dept. of Mathematics, Box 8205, North Carolina State Univ., Raleigh, NC 27695 (e-mail: msolufse@ncsu.edu).

that are embedded in closed-loop cardiovascular models and the breathing mechanics are not patient specific. Our model accounts for individual patient respiration and its effect on heart rate with the incorporation of an electrocardiogram (ECG)-derived respiratory signal, employing algorithms motivated by previous studies (61, 75).

We introduce a novel mathematical model of RSA and baroreflex control mechanisms, modulating heart rate and predicting parasympathetic and sympathetic responses to the VM. The primary objective of this study is to develop a robust model predicting intersubject dynamics during the VM. Using this model, we are able to differentiate dynamics observed in data from 34 control subjects and 5 patients with AD measured during repeated VMs. The 5 AD patients all exhibit the same pressure characteristics [the 'V' response categorized by Palamarchuk et al. (53)] but have different pathologies. This model analyzes how the cardiovascular control system is impacted in each of these patients.

The mathematical techniques used here provide a model-based analysis of the data inferring changes in neurological signaling over time. For patient specificity, our study uses the subject's intrathoracic pressure (ITP) combined with their ECG-derived respiratory signal to determine thoracic pressure. The thoracic pressure modulates heart rate due to respiration and delineates between the aortic and carotid high-pressure baroreceptor (HPB) regions. To our knowledge, this concept has only been used in one previous study (35). We estimate a subset of model parameters fitting the model to individual subject heart rate data, determining a patient-specific neural outflow. Although the use of subset selection and parameter estimation is not new (49), to our knowledge no previous VM studies have taken advantage of these numerical methods. We also compare model-derived quantities with indices extracted directly from the measured systolic blood pressure (SBP) and heart rate data (46, 47), which comprise the baroreceptor sensitivity (β), the Valsalva ratio (γ) (31, 46, 63), and a novel index (α) that we hypothesize is a measure of the subject's sympathetic function. Finally, inspired by previous studies (37, 40, 50), we employ a discrete delay to account for the time it takes to transmit sympathetic signals from the medulla to the effector (heart rate in this case). To our knowledge, this is the first attempt to use this mechanistic modeling approach to analyze autonomic function associated with the VM.

MATERIALS AND METHODS

Valsalva Maneuver

Procedure. The VM is the process associated with forced exhalation against an external resistance, keeping the glottis open (24). The subject maintains an expiratory force for 15 s, increasing the ITP to 40 mmHg, which in turn reduces venous return to the heart (47, 60). The reduced filling of the heart decreases stroke volume, decreasing the blood volume sensed by low-pressure baroreceptors (LPBs) in the venoatrial junctions, the right atrium, and the pulmonary artery as well as the blood pressure sensed by the aortic and carotid HPBs (73). The tonic firing of the nerves conducting signals from these receptors to the brain stem is reduced, causing a shift in the output from the cardiovascular control centers. The net effect is a fast withdrawal of parasympathetic activity to the heart and a slower increase in sympathetic activity to the heart and blood vessels. The efferent response induces cardiac acceleration and vasoconstriction (not modeled in this study). The four distinct phases of the VM marked with alternating gray and light gray boxes in Fig. 1 are as follows:

I. At the onset of the VM, the subject takes a deep breath and initiates the forced expiration. This increases the ITP, causing a sudden increase in blood pressure due to increased transmural pressure on the heart and large arteries. The deep exhalation and subsequent deep inhalation of the breath results in a transient reduction of ITP just before the maneuver, contributing to a temporary decrease in heart rate.

II. As the breath is held, the respiratory-mediated parasympathetic activity decreases. Increased ITP impedes venous blood return to the heart. Blood pressure falls, triggering the baroreflex, which in turn decreases baroreflex-mediated parasympathetic activity. Heart rate initially rises due to parasympathetic with-

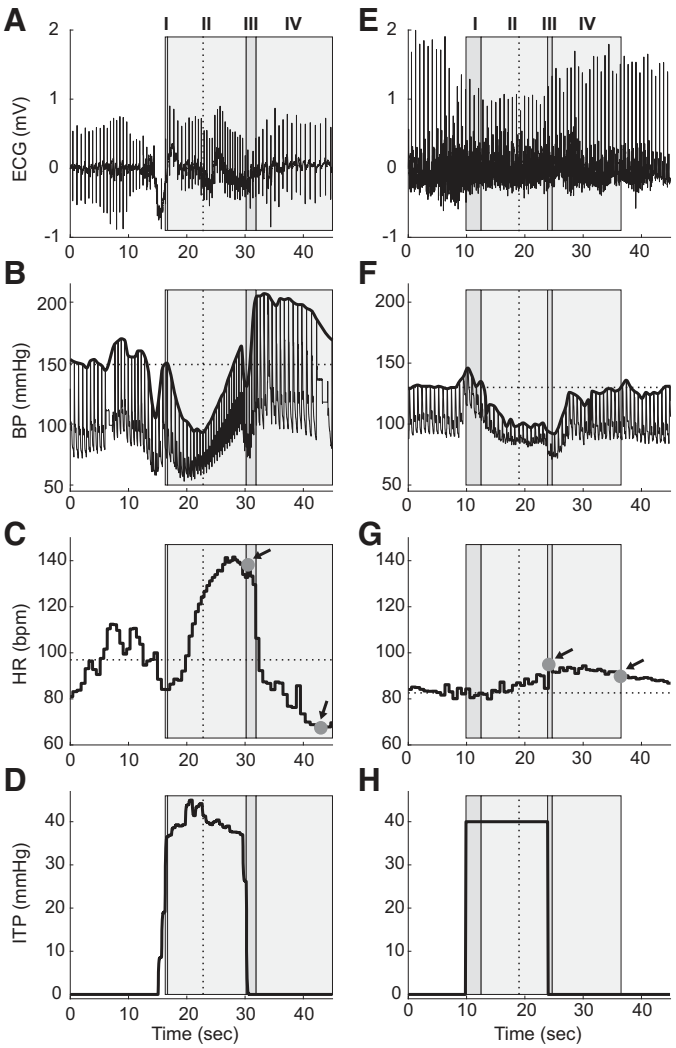

Fig. 1. Valsalva maneuver (VM) data from a representative control subject (*control subject 2*) (*A–D*) and a patient (*E–H*) with the V behavior (*patient 3*) as categorized by Palarmarchuk et al. (52). Alternating gray and light gray boxes indicate phases I–IV of the VM. Early and late phase II are divided with a vertical dotted black line in the light gray phase II block. *A* and *E*: electrocardiogram (ECG, mV) trace. *B* and *F*: blood pressure (BP, mmHg) trace with interpolated systolic blood pressure (SBP, thick curve) and baseline SBP (dotted line). *C* and *G*: heart rate [HR, bpm (beats/min)] trace with baseline HR (dotted line). Maximum HR in phase III and minimum HR in phase IV used in the calculation of γ are indicated with circles. *D* and *H*: intrathoracic pressure (ITP, mmHg) trace. *D*: measured ITP of the control subject from which the VM start and end times, t_s and t_e, respectively, were extracted. *H*: manufactured ITP calculated in *Eq. 4*.

drawal (early phase II) and continues to rise as sympathetic outflow increases (late phase II). Despite the decreased stroke volume, blood pressure gradually returns to pretest levels due to increases in peripheral vascular resistance mediated by sympathetic activity.

III. Upon release of the ITP, the subject typically exhales forcefully. This causes a transient increase in ITP, which further impedes cardiac filling, and hence the preload. The result is a sudden drop in blood pressure. Then, the ITP returns to normal and blood returns to the heart unimpeded.

IV. After normalization of venous return to the heart, the stabilized stroke volume is expelled against an increased vascular resistance causing blood pressure to temporarily overshoot. This overshoot causes a rapid fall in heart rate as the parasympathetic system activates. Breathing returns to normal.

Clinical ratios. Clinicians extract a number of quantities from the SBP and heart rate to determine 'normal ranges' for autonomic function for healthy control subjects (47). In this study, we introduce a novel clinical ratio, α, calculated as

$$\mathrm{SBP} = \alpha t + b, \qquad t \in \left[t_{\mathrm{SBP,min,II}}, t_{\mathrm{SBP,max,II}}\right], \tag{1}$$

where α and b are the slope and the intercept of the regression, respectively, and $t_{\mathrm{SBP,min,II}}$ and $t_{\mathrm{SBP,max,II}}$ are the time points for the minimum and maximum SBP in late phase II, respectively. Figure 2 depicts the calculation of α. We interpret α as an estimate of the vasoconstrictive capacity of the systemic vasculature. A previous study has hypothesized that the use of a metric assessing sympathetic function in late phase II of the VM should be considered (52). To our knowledge, this is the first instance of using α as an approximation of sympathetic nervous function. A popular clinical index is baroreceptor sensitivity (β) (47, 48, 63), calculated as

$$\beta = \frac{\text{max R-R} - \text{min R-R}}{\text{max SBP} - \text{baseline SBP}}, \tag{2}$$

where the numerator is the difference in maximum and minimum R-R intervals in milliseconds and the denominator describes the extent of the overshoot of the SBP. β is a measure of heart rate change given a change in blood pressure (78). It should be noted that this index does not elucidate how changes in the SBP or R-R interval arise. An increase in β can be contributed to an increase in parasympathetic activity, a decrease in sympathetic activity, or a combination of the two (68). Finally, the Valsalva ratio is

$$\gamma = \frac{H_{max,III}}{H_{min,IV}}, \tag{3}$$

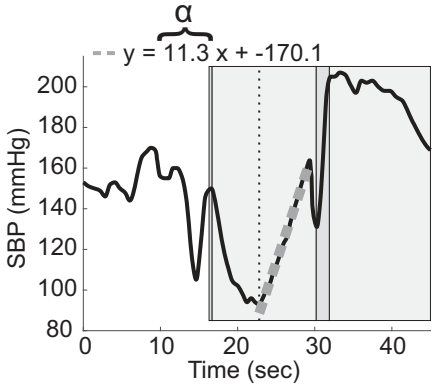

Fig. 2. Depiction of α as the slope of the line of regression of the systolic blood pressure (SBP, mmHg) in late phase II.

Table 1. *Population statistics from the characteristic Valsalva maneuver for 34 control subjects*

Description	Symbol	Population Statistics
Age, yr		32 ± 12
Baseline systolic blood pressure, mmHg	s_w	123 ± 20
Baseline heart rate, beats/min	$\overline{H}$	79 ± 13
Intrinsic heart rate, beats/min	H_I	100 ± 7
Maximal heart rate, beats/min	H_M	185 ± 7
Length of breath hold, s		14 ± 0.7
Max forced expiration, mmHg		37 ± 1

where $H_{max,III}$ is the maximum heart rate in phase III and $H_{min,IV}$ is the minimum heart rate in phase IV (47, 63). γ is typically interpreted as a measure of vagal function with abnormal values below 1.1 (16).

Data and Experimental Design

Data acquisition. Our study analyzes ECG-derived heart rate and respiratory signals, blood pressure, and ITP data from 37 control subjects (24 women and 13 men) and 5 AD patients (1 woman and 4 men). This protocol, "Method study in the Valsalva maneuver" (H-16036257), was approved by the Ethics Committee of the Capital Region, Denmark, and all subjects gave written consent to participate in the study. Of the 37 control subjects, data from 34 (21 women and 13 men) were analyzed in this study. Two subjects were excluded because of pregnancy and one subject was excluded due to data collection error. Table 1 summarizes control subject population statistics.

The 5 AD patients vary in age and diagnosis and were chosen because they all exhibit the V behavior as categorized by Palamarchuk et al. (53), reproducible in repeated intrasubject VM tests. Figure 1*F* shows a typical V behavior characterized by an absent SBP recovery in phase II and an absent SBP overshoot in phase IV. This may occur in adrenergic failure, which does not increase arteriolar resistance (53). In this study, we show that the characteristic V behavior can be caused by parasympathetic or sympathetic dysfunction or both during the VM. *Patient 1* (16 yr old) is diagnosed with postural orthostatic tachycardia syndrome (POTS), characterized by an increase in heart rate ≥40 beats/min (for patients younger than 18 yr) during the head-up tilt test (53). *Patient 2* (79 yr old) is diagnosed with orthostatic hypotension (OH), characterized by a decrease in SBP ≥30 mmHg without associated tachycardia during head-up tilt (53). *Patients 3* (71 yr old) and *4* (83 yr old) have Parkinson's disease (PD). *Patient 5* (75 yr old) is diagnosed with pure autonomic failure (PAF), characterized by OH in conjunction with dramatic SBP changes in response to common activities (9). Table 2 summarizes the patient descriptions.

All tests were performed between 8:00 AM and 3:00 PM under a nonfasting state at standard room temperature. ECG and blood pressure signals were measured continuously at 1,000 Hz from a precordial ECG-lead and by Finometer equipment (Finapres Medical Systems BV, Amsterdam, The Netherlands), respectively. Analog data

Table 2. *Descriptions of patients with autonomic dysfunction displaying the V behavior categorized by Palamarchuk et al. (52)*

Patient	Sex	Age	Diagnosis	Abbreviation
1	Female	16	Postural orthostatic tachycardia syndrome	POTS
2	Male	79	Orthostatic hypotension	OH
3	Male	71	Parkinson's disease	PD
4	Male	83	Parkinson's disease	PD
5	Male	75	Pure autonomic failure	PAF

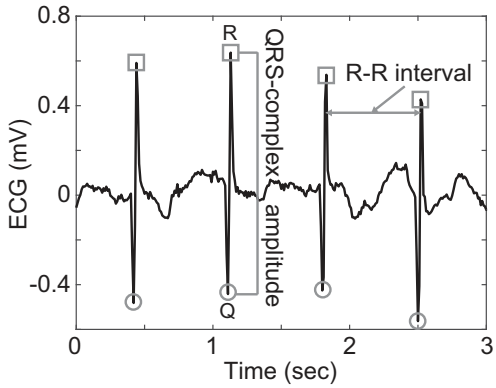

Fig. 3. Electrocardiogram (ECG, mV) with R- and Q-points indicated with squares and circles, respectively. A representative QRS-complex amplitude and R-R interval are indicated.

acquisition was performed, and data were converted to digital format and stored using the LabChart software (LabChart, AD Instruments, Colorado Springs, CO). Figure 1, *A–D*, shows a typical VM data set containing ITP, ECG, blood pressure, and heart rate data for *control subject 2*, and Fig. 1, *E–H*, shows the VM response from *patient 3*. The measurements from the patients are from a previous experiment with a similar protocol. Because these data are collected in real time, the data are inherently noisy.

All tests were performed with the subject in sitting position. The subjects were asked to rest for 5 min before initiating the VM. A mouthpiece was connected to a mercury manometer by a rubber hose with an intercalated differential pressure transmitter (DTP-7000-R8, HK Instruments, Muurame, Finland). The subjects were asked to take a deep inspiration and then blow into the mouthpiece, trying to reach and maintain a steady forced expiration at 40 mmHg for 15 s. For the control subjects, ITP was collected continuously (Fig. 1*D*). For the AD patients, ITP was measured and verified by visual inspection. We assume the patients maintain a constant expiratory force of 40 mmHg for the duration of the breath hold, given as

$$\mathrm{ITP}_j = \begin{cases} 40 & t_s \le t_j \le t_e \\ 0 & \text{otherwise} \end{cases}, \tag{4}$$

where ITP_j is the intrathoracic pressure at time t_j, t_s is the start time of the breath hold determined by the sharp increase in SBP in phase I, and t_e is the time the breath hold is released in phase III. Figure 1*H* depicts the estimated ITP signal in *Eq. 4*. Each subject performed multiple repetitions of the VM with 2 min between maneuvers. Time-series ECG, blood pressure, ITP, and heart rate signals were extracted from LabChart for all viable VMs from each subject, that is, a data set in which the VM was performed correctly (i.e., the subject reached ~40 mmHg immediately and held that pressure steady with ± 5 mmHg). All subjects with the exception of *control subject 20* and *patients 2* and *4* had more than one VM data set. Heart rate was computed from R-R intervals using LabChart cyclic detection for human ECG.

Data preprocessing. The open-loop model formulated in this study is a system of differential equations solved numerically using a variable-step stiff delay solver, RADAR5 (20). Because the model equations are a function of SBP and thoracic pressure, we interpolate the data to evaluate the model. We interpolate SBP, the apex of the pulse pressure signal in one heartbeat, over every cardiac cycle. Following Arndt et al. (2), the average discharge of the baroreceptor neurons correlates with systolic, diastolic, and mean blood pressures. To be consistent with the clinical ratios calculated in this study, we chose to predict wall strain modulating the baroreflex as a function of SBP. We used the piecewise cubic Hermite interpolating polynomial (PCHIP) algorithm in MATLAB 2018a to ensure monotonicity of the interpolation and preserve local extrema in the data (17).

The amplitude of the ECG gives an indication of the depth of the breath. As the subject inhales, the chest expands and the electrodes on the skin move away from the heart. An ECG-derived respiratory signal can be determined from the interpolation of the amplitude of the QRS-complex in the ECG, as shown in Fig. 3. We developed a protocol employing algorithms from previous studies (61, 70, 75). Widjaja et al. (75) validated this procedure against a measured reference respiratory signal at rest and under mental stress. We found local optima (i.e., the R- and Q-points) to determine the amplitude of each QRS-wave and interpolated the values. Similar to the SBP, the QRS-complex occurs once per cardiac cycle, and the sparsity of the data requires a careful choice in interpolation scheme. Therefore, the only deviation we made from the developed algorithms is using PCHIP. The resulting interpolated QRS-complex amplitude is assumed to be the mechanical breathing signal (Fig. 4*B*).

Because the ECG-derived respiratory signal may miss obstructive apnea episodes, which can occur during the VM (25), we compute the thoracic pressure (P_{th}) by combining the effect from respiration at rest with ITP data measured during the VM as

$$P_{th,j} = \begin{cases} \mathrm{ITP}_j & t_s \le t_j < t_e \\ \dfrac{R_M - R_m}{\bar{R}_I - \bar{R}_E} R_j + \left(R_m - \bar{R}_E\right) & \text{otherwise} \end{cases}, \tag{5}$$

where $R_M = 6$ and $R_m = 3.5$ are the maximal and minimal breathing amplitudes (23); $\bar{R}_I$ and $\bar{R}_E$ are the mean amplitudes calculated from the data for the end of inspiration and end of expiration; and $\bar{R}_I$ and $\bar{R}_E$ are the mean amplitudes calculated from the respiration data for the end of inspiration and end of expiration. t_s and t_e denote the start and end of the VM. The bottom term is valid under the assumption that respiration is linearly related to P_{th}. This is motivated by Kobayshi's (33) observation that at rest the RSA is linearly related to tidal volume and the assumption that tidal volume is linearly related to P_{th}. This signal was then filtered using the "movmean" command in MATLAB 2018a, which calculates a moving average over a specified window. In this study, we used a 1-s window.

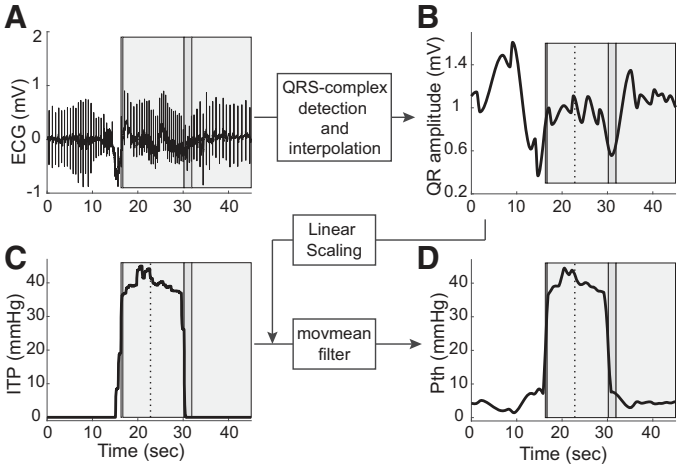

Fig. 4. Thoracic pressure (P_{th}) input schematic. QRS-complexes are detected in the electrocardiogram (ECG, mV) trace (*A*). Amplitudes of consecutive QRS-complexes are interpolated using a piecewise cubic Hermite interpolating polynomial. This signal is filtered to produce the respiration signal (*B*), which is in turn scaled linearly given in *Eq. 5*. The intrathoracic pressure (ITP, mmHg) trace (*C*) is combined with the scaled respiration curve and filtered using the "movmean" command in MATLAB 2018a to produce P_{th} (*D*).

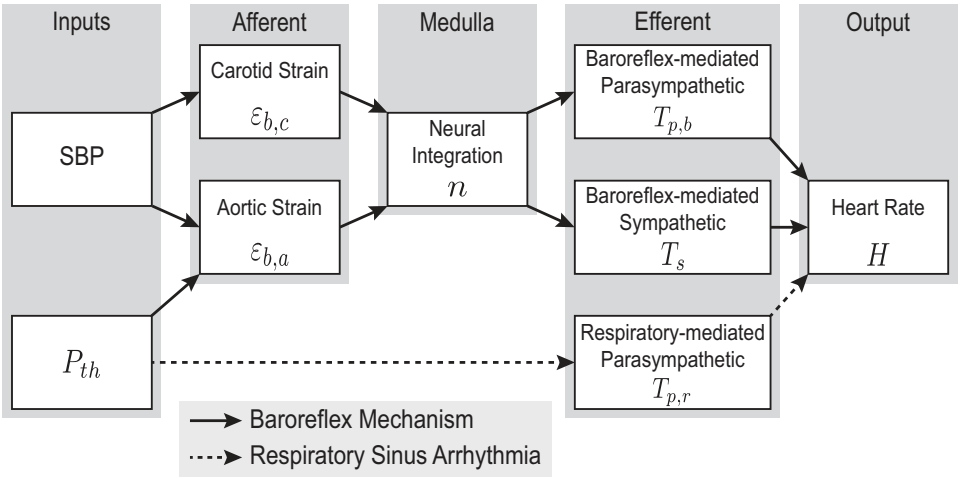

Fig. 5. Schematic of the model with the systolic blood pressure (SBP, mmHg) and thoracic pressure (P_{th}, mmHg) as inputs. The baroreflex mechanism (solid arrows) and respiratory sinus arrhythmia (RSA, dotted arrows) are shown. Afferent signals are transmitted to the medulla via the carotid baroreceptor strain ($\varepsilon_{b,c}$), stimulated solely by the SBP, and the aortic baroreceptor strain ($\varepsilon_{b,a}$), stimulated by the difference in the SBP and P_{th}. The signals from the carotid sinus and aortic arch are integrated in the medulla via the neural integration, n. The baroreflex activates parasympathetic ($T_{p,b}$) and sympathetic (T_s) efferent signals, which modulate the heart rate output (H). P_{th} also modulates H during normal breathing via RSA($T_{p,r}$).

Model Development

The model developed in this study (Fig. 5) takes SBP and P_{th} as inputs and generates heart rate (H) as the output. The model encoding two control mechanisms, the baroreflex and RSA, has four major components: *1*) an afferent baroreflex component, inspired by (42); *2*) a neural integration component combining aortic and carotid afferent signals; *3*) an efferent baroreflex component encompassing the baroreflex-mediated parasympathetic and sympathetic outflows; and *4*) an efferent respiratory component modulating parasympathetic outflow. These components combine to determine H. The model developed below has 6 interacting state variables with 26 parameters.

Pressure signals. Increased ITP and forceful exhalation characterize the VM. Previous studies have posed mathematical models for inducing ITP by using a discrete step function (26, 40) or piecewise-continuous functions (30, 59). In this study, we use the P_{th} given in *Eq. 5*. Since the arterial blood pressure data is from the finger (outside the thorax), we assume that it does not account for effects of the fluctuating ITP. Because the model is zero-dimensional (i.e., the equations only depend on time), we neglect the reflected waves, which augment arterial SBP (45). Therefore, we assign the continuous interpolated SBP to be the blood pressure sensed by the carotid sinus (P_c). We assume the pressure exerted on the tissues as the thoracic cavity inflates is negligible. Conversely, the aortic baroreceptors are inside the thorax and do experience increased ITP. We express the aortic blood pressure (P_a) as the difference between the SBP and P_{th}. These interactions are summarized with the following equations:

$$P_c = \text{SBP and } P_a = \text{SBP} - P_{th}, \tag{6}$$

where SBP denotes the interpolated SBP and P_{th} is as in *Eq. 5*.

Arterial wall deformation. HPBs are embedded in the tunica externa of the arterial wall, surrounded by collagen fibers and supported by elastic laminae (7). Blood pressure and change in blood pressure deform and distend the arterial wall, causing HPBs to fire. Strain increases as pressure increases (72). Since HPBs are found in both carotid and aortic regions with little to no variation between cells, we model the arterial wall strain ($\varepsilon_{w,j}$) as

$$\varepsilon_{w,j} = 1 - \sqrt{\frac{1 + e^{-q_w(P_j - s_w)}}{A + e^{-q_w(P_j - s_w)}}}, \tag{7}$$

where P_j is the pressure sensed by the arterial wall for $j = a$ or c for aortic or carotid, respectively. The parameters q_w (mmHg^{-1}) and s_w (mmHg) denote the steepness and half-saturation value of the sigmoidal relationship in *Eq. 7*. A (dimensionless) denotes the maximum to unstressed cross-sectional area ratio (42).

High-pressure baroreceptor stimulation. Carotid baroreceptor nerve fibers form bundles of myelinated and unmyelinated fibers embedded in the collagen. As the vessel wall deforms, the HPBs stretch and return to rest. Collagen gives rise to viscoelastic deformation (71). Given that the baroreceptor nerve endings are embedded in collagen, it is natural to hypothesize that, due to their viscoelastic nature, baroreceptor deformation exhibits hysteresis, i.e., the baroreceptors respond differently to an increase in wall strain as opposed to a decrease (21).

To model this behavior, we compute baroreceptor strain ($\varepsilon_{b,j}$) using Voigt body elements represented by a dashpot and resistor in parallel, mimicking the viscoelastic properties of the arterial wall (18). A schematic of one Voigt body element is shown in Fig. 6, where the Voigt body deforms due to pressure-dependent changes in arterial wall strain $\varepsilon_{w,j}$. Inspired by previous studies (10, 42), we model the stress-strain relationship for one Voigt Body element as

$$\eta_1 \frac{d\varepsilon_{b,j}}{dt} + \mu_1 \varepsilon_{b,j} = \mu_0 \varepsilon_{w,j}, \tag{8}$$

where μ_0 (dimensionless) is the spring proportionality constant for the spring in series with the Voigt body and η_1 (s) and μ_1 (dimensionless) are the dashpot and spring proportionality constants, respectively, for $j = c$ or a. Assuming μ_0, μ_1, and η_1 are not region specific, the baroreceptor nerve fibers are inherently the same in both regions. Similar to previous studies (10, 37, 40), we simplify *Eq. 8* by combining parameters and obtaining a linear differential equation predicting $\varepsilon_{b,j}$ as a function of $\varepsilon_{w,j}$ of the form

$$\frac{d\varepsilon_{b,j}}{dt} = \frac{-\varepsilon_{b,j} + K_b \varepsilon_{w,j}}{\tau_b}, \tag{9}$$

where $K_b = \mu_0/\mu_1$(dimensionless) and $\tau_b = \eta_1/\mu_1$ (s) are the gain and time constant of the HPB strain, respectively.

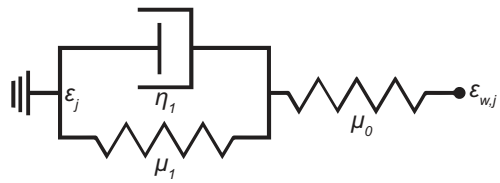

Fig. 6. Voigt body element of the baroreceptor strain (ε_j) for $j = c$ or a, indicating carotid and aortic regions, respectively, as they deform due to the arterial wall strain ($\varepsilon_{w,j}$). The baroreflex strain is predicted using one Voigt body element and a spring in series with spring proportionality constants (μ_0 and μ_1) and dashpot proportionality constant (η_1).

Neural integration. Carotid baroreceptors transduce signals via the glossopharyngeal nerve, and aortic baroreceptors transduce signals via the vagal nerve (7). The nerves synapse in the nucleus of the solitary tract, which integrates and transmits the signals to the appropriate medullary region to elicit an efferent response (7). Little is known about how the information from various regions of the vasculature are integrated and whether the medulla prefers one signal type to another. We do not model firing of individual neurons, but rather define neural integration (n) as a convex combination of the transduced HPB signals in response to the relative strain of each component, i.e.,

$$n = B\left(\varepsilon_{w,c} - \varepsilon_{b,c}\right) + \left(1 - B\right)\left(\varepsilon_{w,a} - \varepsilon_{b,a}\right), \quad B \in \left[0, 1\right]. \quad (10)$$

The model output depends solely on carotid HPB stimulation if $B = 1$ and aortic HPB simulation if $B = 0$.

Efferent baroreflex response. The nucleus ambiguus is the primary determinant of the fast baroreflex-mediated parasympathetic response ($T_{p,b}$), sending efferent signals via the vagal nerve to the heart (7). The rostral ventrolateral medulla governs the baroreflex-mediated sympathetic response (T_s) via the sympathetic ganglia chain to the heart. Although previous studies have found an empirical sympathetic delay of 1.7 s in dogs (5) and 1.06 s in rabbits (6), previous modeling studies have used a 3- (40, 74) and 4-s (36) delay for humans. We chose to remain consistent with these modeling studies, using a delay of 3 s. $T_{p,b}$ arrives at the sinoatrial node much faster than T_s, and we assume the delay in $T_{p,b}$ is negligible. To maintain the inherent nonlinearity and hysteretic behavior of the neural outflows, we employ sigmoid functions of the form

$$G_{p,b} = \frac{1}{1 + e^{-q_{p,b}\left(n - s_{p,b}\right)}} \text{ and } G_s = \frac{1}{1 + e^{q_s\left(n - s_s\right)}}, \quad (11)$$

where n (s^{-1}) is as in *Eq. 10* and q_l (s) and s_l (s^{-1}) are the steepness parameter and half-saturation value with $l = p,b$ or s for parasympathetic and sympathetic baroreflex effects, respectively. We compute $T_{p,b}$ and T_s as the solutions to the first-order linear differential equations

$$\frac{dT_{p,b}}{dt} = \frac{-T_{p,b} + K_{p,b}G_{p,b}}{\tau_{p,b}} \text{ and } \frac{dT_s}{dt} = \frac{-T_s\left(t - D_s\right) + K_sG_s}{\tau_s}, \quad (12)$$

where K_l (dimensionless) and τ_l (s) are the gain and time constants. D_s (s) is the delay in signal transmission of the sympathetic outflow. $T_{p,b}$ and T_s are dimensionless quantities modeling the outflow of the autonomic nervous activity in response to the afferent baroreflex firing rate.

Efferent respiratory pathway. The control centers of the respiratory muscles and heart rate are in close proximity in the brain stem and interact strongly (64). One such mechanism is RSA, or heart rate variability in synchrony with respiration (77). RSA is most prominent at rest, mediated via the vagal nerve synapsing on the sinoatrial node (78). Many factors influence RSA, one being LPBs known to modulate heart rate at rest (7). Note that LPBs do not give rise to RSA but may modify its effects. LPBs deactivate during phases I and II, reactivate in phase III, and help return heart rate to baseline in phase IV. LPBs sense changes in central blood volume in the vena cava and right atrium (7). However, because these volume measurements are difficult to acquire without performing invasive experiments, we used the ECG-derived respiratory signal in lieu of modeling LPBs explicitly.

The respiratory center receives stimuli from autonomic afferents and the cerebral cortex. Therefore, respiration can be controlled both voluntarily and involuntarily. Consequently, the model has a solely efferent respiratory-mediated component, with P_{th} as the input, modeled as a decreasing sigmoid to account for the saturation of the thoracic pressure during large breaths in the form

$$G_{p,r} = \frac{1}{1 + e^{q_{p,r}\left(P_{th} - s_{p,r}\right)}}, \quad (13)$$

where $q_{p,r}$ ($mmHg^{-1}$) and $s_{p,r}$ (mmHg) are the steepness and half-saturation value of the sigmoid, respectively. The respiratory-mediated parasympathetic outflow ($T_{p,r}$) is the solution of the differential equation

$$\frac{dT_{p,r}}{dt} = \frac{-T_{p,r} + K_{p,r}G_{p,r}}{\tau_{p,r}}, \quad (14)$$

where $K_{p,r}$ (dimensionless) and $\tau_{p,r}$ (s) are the gain and time constants, respectively. The respiratory center does relay sympathetic nervous system signals, but these signals do not synapse on the sinoatrial node (78). Therefore, a respiratory-mediated sympathetic efferent is not included in this study.

Heart rate. Based on our previous studies (49–51), we model the resting heart rate as a linear combination of the efferent responses as

$$\tilde{H} = H_I\left(1 - H_{p,b}T_{p,b} + H_{p,r}T_{p,r} + H_sT_s,\right) \quad (15)$$

where H_I (min^{-1}) is the intrinsic heart rate, $H_{p,b}$ and H_s (dimensionless) are scaling parameters for the baroreflex-mediated parasympathetic and sympathetic heart rate components, respectively, and $H_{p,r}$ (dimensionless) is the scaling parameter for the respiratory-mediated parasympathetic heart rate component. Previous models included a multiplicative term, incorporating the cancellation that occurs with both the parasympathetic and sympathetic baroreflex-mediated signals (40, 51). However, simulations (not shown) indicate that this term does not affect the model output substantially. The intrinsic heart rate is the natural beating frequency of the denervated heart calculated as a function of age (29). RSA-mediated parasympathetic activity only acts to increase H, as resting expiration is passive; hence, the positive sign before $H_{p,r}$ in *Eq. 15*. In response to a stressor, such as the VM, the dynamic heart rate is the solution to the differential equation

$$\frac{dH}{dt} = \frac{-H + \tilde{H}}{\tau_H}, \quad (16)$$

where τ_H (s) is the time constant for the response.

In summary, the model defined above is a system of stiff delay differential equations of the form

$$\frac{dx}{dt} = f\left(t, x\left(t\right), x\left(t - D_s\right); \theta\right), \quad (17)$$

where $x = \left[\varepsilon_{b,c},\varepsilon_{b,a},T_{p,b},T_{p,r},T_s,H\right]^T$ denotes the vector of 6 model states, D_s denotes the discrete sympathetic delay, and $\theta \in \mathbb{R}^{26}$ denotes the vector of model parameters. The input of the model is the SBP and P_{th} signals, and the output for this model is the heart rate state H.

Nominal parameter values and initial conditions. The neural model described above has a total of 26 parameters, including

$$\theta = [A, B, K_b, K_{p,b}, K_{p,r}, K_s, \tau_b, \tau_{p,b}, \tau_{p,r}, \tau_s, \tau_H, \ldots$$
$$q_w, q_{p,b}, q_{p,r}, q_s, s_w, s_{p,b}, s_{p,r}, s_s, H_I, H_{p,b}, H_{p,r}, H_s, D_s, t_s, t_e]^T. \quad (18)$$

Table 3 summarizes the parameters and their descriptions, units, source from literature (if applicable) and nominal values. For parameter values calculated from the data, we give the mean and one standard deviation with the corresponding equation number. A detailed discussion of nominal parameters assignments is in the APPENDIX. The parameters t_s and t_e come from the ITP data as the time points of greatest ITP change. The nominal value for the neural scaling factor B was set to 0.5, assuming the aortic and carotid signals are averaged in the medulla. The sigmoid half-saturation values, s_w, $s_{p,b}$, $s_{p,r}$, and s_s, approximately correspond to baseline values. s_w and $s_{p,r}$ can be interpreted as the baseline SBP and P_{th} averaged over 15 s at rest. We

Table 3. *Summary of parameter values and their descriptions, units, source (if any), and nominal values*

Description and Symbol	Units	Source					
		Mahdi et al. (42)	Lu et al. (40)	Ottesen (50a)	Olufsen et al. (50)	Wesseling and Settels (74)	This Study
Cross-sectional area ratio (A)		5					5
Neural scaling factor (B)	s^{-1}						0.5
ODE Gains							
Afferent baroreceptor (K_b)				1*	3.06*		0.1
Baroreflex parasympathetic ($K_{p,b}$)			0.8*		1*	0.83*	5
Respiratory parasympathetic ($K_{p,r}$)						1.42	1
Baroreflex sympathetic (K_s)			1*		1*	0.48*	5
Heart rate gains							
Intrinsic heart rate (H_I)	min^{-1}		35*		100		100 ± 7 (*A11*)
Baroreflex parasympathetic ($H_{p,b}$)			32*		0.45		0.5 ± 0.2 (*A15*)
Respiratory parasympathetic ($H_{p,r}$)							0.3 ± 0.4 (*A14*)
Baroreflex sympathetic (H_s)			140*		0.99		0.3 ± 0.4 (*A1*)
ODE Time constants							
Baroreceptor strain (τ_b)	s		1	0.5	0.6		0.9
Baroreflex parasympathetic ($\tau_{p,b}$)	s		1.8		1.32	1.8	1.8
Respiratory parasympathetic ($\tau_{p,r}$)	s					6	6
Baroreflex sympathetic (τ_s)	s		10		0.72*	10	10
Heart rate (τ_H)	s				1		0.5
Sigmoid steepness							
Arterial wall strain (q_w)	$mmHg^{-1}$	5*					0.04
Baroreflex parasympathetic ($q_{p,b}$)	s		0.04*				10
Respiratory parasympathetic ($q_{p,r}$)	$mmHg^{-1}$						1
Baroreflex sympathetic (q_s)	s		0.09*				10
Half-saturation values							
Arterial wall strain (s_w)	mmHg	145*					123 ± 20 (*A9*)
Baroreflex parasympathetic ($s_{p,b}$)	s^{-1}		110*				0.54 ± 4e-4 (*A10*)
Respiratory parasympathetic ($s_{p,r}$)	mmHg						4.88 ± 0.21 (*A9*)
Baroreflex sympathetic (s_s)	s^{-1}		100*				0.05 ± 4e-4 (*A10*)
Sympathetic delay (D_s)	s		3		6.12	3	3
Valsalva start time (t_s)	s						data
Valsalva end time (t_e)	s						data

An empty entry in the Units column indicates that the parameter is dimensionless. Some parameters are calculated a priori and the equation reference is provided. Data refers to quantities extracted directly from intrathoracic pressure data. ODE, ordinary differential equation. *Parameter values from models that are scaled differently than the model in this study.

calculated the baroreflex-mediated parasympathetic ($s_{p,b}$) and sympathetic (s_s) baseline values under the assumption that at rest 80% of the baroreflex control of heart rate is due to parasympathetic activity and 20% sympathetic activity (34). The sympathetic heart rate coefficient, H_s, can be determined from the maximum heart rate based on the age of the subject (69). The initial conditions were solved analytically to ensure the model began in steady state, since we assume that the subject is at rest before the VM. Further information on calculations of the initial conditions of the differential equations are in the APPENDIX.

Numerical methods. The model was solved using the RADAR5 algorithm, a stiff delay differential equations solver, in Fortran [developed by Guglielmi and Hairer (20)]. This system is stiff due to the steep, fast-changing sigmoidal relationships given in *Eqs. 7*, *11*, and *13* and the time constants (τ_b, $\tau_{p,b}$, $\tau_{p,r}$, τ_s, and τ_H) varying significantly in magnitude. RADAR5 is an extension of Radau IIA methods, which use explicit Runge-Kutta methods that are suitable for stiff delay differential equation systems. This is a variable-step solver, in which the solution is not necessarily computed at the same times as the experimental data. Hence, the model output was numerically interpolated at the time points of the heart rate data.

Model Analysis

We performed a local analysis on the model residual

$$\boldsymbol{r}(t_j) = \frac{H(t_j;\theta) - H_{data}(t_j)}{H_{data}(t_j)} \frac{1}{\sqrt{N}} \tag{19}$$

evaluated at known (nominal) parameter values (14, 15, 41, 42). Here, $H(t_j; \theta)$ and $H_{data}(t_j)$ denote the heart rate model output and data at time t_j, and N is the number of data points. Because of the variation in magnitude of the parameters, we compute the sensitivity of the model residual to the logarithm of parameter θ_i at time t_j as

$$\boldsymbol{S}_{ij} = \frac{\mathrm{d}\boldsymbol{r}(t_j)}{\mathrm{d}\log\theta_i} = \frac{\mathrm{d}}{\mathrm{d}\theta_i} \frac{H(t_j;\theta) - H_{data}(t_j)}{H_{data}(t_j)} \theta_i = \frac{\mathrm{d}H(t_j;\theta)}{\mathrm{d}\theta_i} \frac{\theta_i}{H_{data}(t_j)}, \tag{20}$$

which is dimensionless. To rank the parameters, we compute the Euclidean norm on each column of $\boldsymbol{S}$

$$s_i = \|\boldsymbol{S}_i\|_2 \tag{21}$$

and then divide all of the column indices by the maximum value, i.e., the most influential parameter has sensitivity 1 (Fig. 7). The integration tolerance for these models was set to $\varphi = 10^{-8}$. The most sensitive parameters are above the sensitivity threshold $10\sqrt{\varphi} = 10^{-3}$ (58).

Many methods exist to perform subset selection identifying a set of uncorrelated parameters that can be estimated given a model and data. Local methods include the structured correlation method (49), subspace selection (66), and singular value decomposition followed by QR factorization (SVD-QR) of the Fisher Information Matrix $\boldsymbol{F} = \boldsymbol{S}^T\boldsymbol{S}$ (49). In this study, we use the structured correlation method to determine a correlation-free subset, which we subsequently verify using the SVD-QR decomposition of $\boldsymbol{F}$. We compute the covariance matrix $\boldsymbol{C} = (\boldsymbol{S}^T\boldsymbol{S})^{-1}$ with corresponding correlation matrix $\boldsymbol{c}$ as

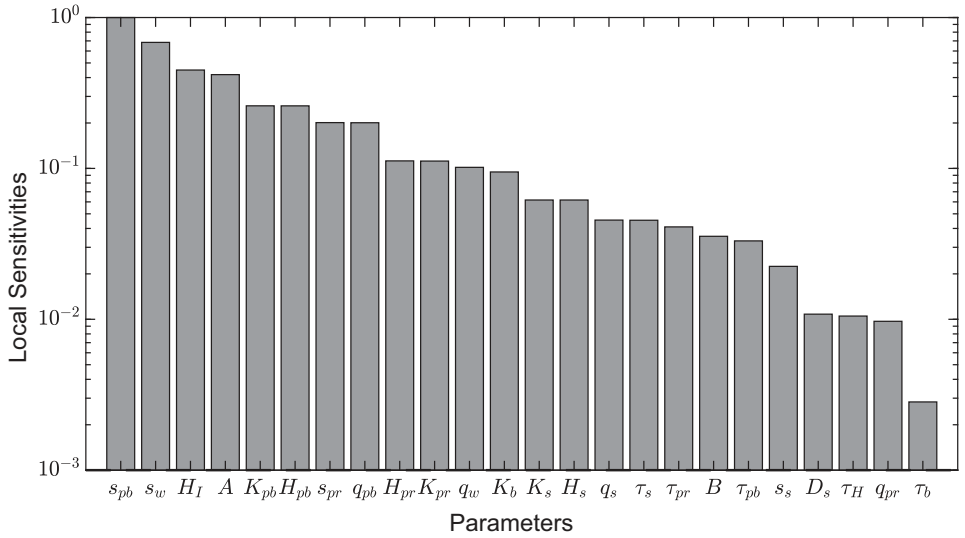

Fig. 7. Ranked relative sensitivities for all parameters excluding the start (t_s) and end (t_e) Valsalva maneuver times. The most sensitive parameter is on the left, and the sensitivities decrease accordingly. All parameters are above the sensitivity threshold of 10^{-3}. A, cross-sectional area ratio; B, neural scaling factor; D_s, sympathetic delay; H_I, intrinsic heart rate; $H_{p,b}$, baroreflex parasympathetic gain controlling heart rate; $H_{p,r}$, respiratory parasympathetic gain controlling heart rate; H_s, baroreflex sympathetic gain controlling heart rate; K_b, afferent baroreceptor gain; $K_{p,b}$, baroreflex parasympathetic gain; $K_{p,r}$, respiratory parasympathetic gain; K_s, baroreflex sympathetic gain; $q_{p,b}$, baroreflex parasympathetic sigmoid steepness; $q_{p,r}$, respiratory parasympathetic sigmoid steepness; q_w, arterial wall strain sigmoid steepness; q_s, baroreflex sympathetic sigmoid steepness; $s_{p,b}$, baroreflex parasympathetic half-saturation value; $s_{p,r}$, respiratory parasympathetic half-saturation value; s_s, baroreflex sympathetic half-saturation value; s_w, arterial wall strain half-saturation value; τ_b, baroreceptor time-scale; $\tau_{p,b}$, baroreflex parasympathetic time-scale; $\tau_{p,r}$, respiratory parasympathetic time-scale; τ_H, heart rate time-scale; τ_s, baroreflex sympathetic time-scale.

$$c_{i,j} = \frac{C_{i,j}}{\sqrt{C_{i,i}C_{j,j}}} \tag{22}$$

to determine a subset of parameters to fit H to the heart rate data. With a covariance threshold of $|c_{i,j}| \geq 0.95$, we obtained a subset of uncorrelated parameters

$$\tilde{\theta} = \left[B, \tau_{p,b}, \tau_{p,r}, \tau_s, H_{p,b}, H_{p,r}, H_s\right], \tag{23}$$

which was verified using the SVD-QR decomposition of $\boldsymbol{F}\left(\tilde{\theta}\right) = \boldsymbol{S}\left(\tilde{\theta}\right)^T \boldsymbol{S}\left(\tilde{\theta}\right)$. Because these methods are local (they analyze correlations at known parameter values), we use a Bayesian approach to verify the subset over the entire parameter space. This is done by mapping pairwise parameter distributions estimated using the delayed rejection adaptative metropolis (DRAM) algorithm (22) (described in the APPENDIX). The tables for parameter values for all data sets may be accessed in the Supplemental Material (All Supplemental Material is available at https://doi.org/10.5281/zenodo.3234934). Parameters that hit their bounds are marked with an asterisk.

We estimated $\tilde{\theta}$ using nonlinear least squares optimization because the problem is nonlinear with respect to the parameters. To estimate the parameter subset, we minimize the least squares cost functional

$$J = \boldsymbol{r}^T\boldsymbol{r} + \left(\frac{\max_j H\left(t_j;\theta\right) - \max_j H_{data}\left(t_j\right)}{\max_j H_{data}\left(t_j\right)}\right)^2, \tag{24}$$

where $\boldsymbol{r}$ is the residual vector given in *Eq. 19* and the second term ensures that the maximal heart rate is predicted accurately. To account for the wide variation in magnitude of the parameters and ensure positivity, we optimized the logarithm of the parameters. We used a Levenberg-Marquardt scheme by Kelley (32). A more detailed description of the model analysis is included in the APPENDIX.

Characteristic VM. Because almost every subject has multiple viable VM data sets, we identify a 'characteristic VM' defined as the VM with estimated and calculated parameter values closest to the intrasubject mean for the subject. The following algorithm determines the characteristic VM for each subject:

1. For each viable VM data set j of the ith subject, we consider the subset

$$\Theta_{i,j} = \left[\tilde{\theta}^T, s_w, s_{p,r}, \overline{H}\right]^T = \left[B, \tau_{p,b}, \tau_{p,r}, \tau_s, H_{p,b}, H_{p,r}, H_s, s_w, s_{p,r}, \overline{H}\right]^T, \tag{25}$$

   which includes the optimized parameter set $\tilde{\theta}$, the baseline blood pressure and P_{rh} values (s_w and $s_{p,r}$), and the baseline heart rate ($\overline{H}$). s_w, $s_{p,r}$, and $\overline{H}$ are used because they are calculated directly from the data and are patient specific. If an optimized parameter hit a lower or upper bound, that value was excluded. We calculate the intrasubject means of these parameters, $\bar{\Theta}_i$.
2. Because the parameters vary in scale, we compare the logarithm of the parameters. We determine which VM data set is characteristic for that subject by

$$\min_j \|\log\bar{\Theta}_i - \log\Theta_{i,j}\|_2. \tag{26}$$

3. The viable VM data set with $\Theta_{i,j}$ closest to the mean is the characteristic VM for that subject.

RESULTS

We have validated our model against 34 control subjects and 5 AD patients with V behavior categorized by Palamarchuk et al. (52). For each subject, we fitted the model to every VM data set and identified a characteristic VM. We used the Levenberg-Marquardt optimization algorithm (32) to estimate the identifiable parameter subset $\tilde{\theta}$ given in *Eq. 23*, minimizing the least squares error given in *Eq. 24*. Table 4 lists the population means and SDs of the clinical ratios for the control subjects, calculated from the characteristic VM for each subject, and the

Table 4. *Clinical ratios for the control group and the 5 patients with autonomic dysfunction*

	Clinical Ratios		
	α	β	γ
Control (34 subjects)	5 ± 3	15 ± 13	1.7 ± 0.4
Patient			
1	−0.6*	19	2.3*
2	0*	3	1*
3	0*	13	1.1*
4	0*	18	1*
5	0.5*	3*	1*

Values are means and SDs. Pathologies are listed in Table 1. α, adrenergic function from the slope of the systolic blood pressure in phase II (a novel index); β, baroreceptor sensitivity; γ, Valsalva ratio. *Clinical ratio is outside of 1 SD.

clinical ratios for each AD patient. Table 5 lists the population means and SDs for the estimated parameter values for the control subjects along with the values for the 5 AD patients. Model fits and predictions for each data set are given in the Supplemental Material (available at https://doi.org/10.5281/zenodo.3234934).

To test identifiability of the parameters in subset $\tilde{\theta}$, we varied the nominal parameter values in *Eq. 21* by ± 20% for 10 optimization iterations for *control subject 2*. The mean (μ) and SDs (σ) were calculated across the iterations. The coefficient of variation σ/μ for each parameter in subset $\tilde{\theta}$ did not exceed 0.14 (results of the convergence analysis can be found in the Supplemental Material). This was performed on the characteristic VM for each subject with similar results, indicating the scheme had reached an individual minimum.

Sensitivity Analysis

Qualitative behavior. Figure 7 displays the model performance (computed with optimized patient-specific parameters) for a representative control subject (*subject 2*) and all 5 AD patients. Figure 8 displays the input signals SBP and P_{th} (column 1, row 1) used to distinguish the afferent HPB strains of the carotid sinus (dark curve) and aorta (light curve) (column 1, row 2). These signals modulate the efferent baroreflex-mediated parasympathetic ($T_{p,b}$, dark curve) and sympathetic (T_s, light curve) responses (column 1, row 3). The ordinates of the plot can be interpreted as a percentage of the autonomic outflow. Column 1, row 4 displays the respiratory-mediated parasympathetic outflow ($T_{p,b}$). The model output H (gray) is effectively calibrated to the heart rate data (black) both at rest and during the VM (column 1, row 5). The large oscillations in the heart rate data are due to deep inhalations of the subject before the VM, which are captured by the respiratory model component. All signals begin in steady-state when the subject is at rest. Since the model output is continuous and the data are discrete, inevitably there will be discrepancies between each individual heart period and the model output.

The 5 AD patients all have different pathologies, noted at the top of columns 2–6, that result in different control responses from the baroreflex and RSA. *Patient 1* is diagnosed with POTS, as shown with the substantial increase in heart rate. By comparing column 1 row 3 (control) to column 2 row 3 (POTS), the model predicts overactive parasympathetic and sympathetic behavior. $T_{p,b}$ (dark curve) oscillates significantly more at steady state and decreases to zero during the VM. T_s (light curve) increases substantially during late phase II of the VM, then decreases sharply in phase III, and undershoots in phase IV. Dynamic regulation from RSA is minimal (column 2, row 4), as $T_{p,r}$ is a smooth curve with minor fluctuations.

In comparison, *patients 2–5* (columns 3–6, row 3) have a suppressed parasympathetic response to the control subject and *patient 1* (columns 1 and 2, row 3). Because these patients are much older than the control subject and *patient 1*, they are expected to have decreased $T_{p,b}$ activity (55). The traces for T_s behave similarly to the control subject. This is surprising, especially for *patient 5*, as PAF typically displays substantial adrenergic sensitivity (9). These results suggest that for these patients there is a substantial decrease in parasympathetic activity, whereas their sympathetic activity to the sinoatrial is normal.

Similarly, we expect $T_{p,r}$ (the respiratory outflow) to exhibit minimal dynamics. However, for *patients 3*, *4*, and *5*, $T_{p,r}$ fluctuates similar to the control subject. The trace for $T_{p,r}$ must be taken in conjunction with the RSA gain for the heart rate $H_{p,r}$ (Table 5). Even though $T_{p,r}$ is dynamic for *patients 3*, *4*, and *5*, $H_{p,r}$ is 0.02, 0.09, and 0.03, respectively, indicating little to no effect of RSA on heart rate. Hence, the model is able to produce a trace for RSA, which can represent respiratory effects in these patients that are not reflected in the heart rate.

Quantitative Results

Clinical ratios. Table 4 lists the means and SDs of the clinical ratios for the characteristic VMs for all 34 control subjects and 5 AD patients. To test if extracted clinical ratios vary with age or sex, we divided the control group by sex (male

Table 5. *Cost functional and estimated parameter values for the characteristic Valsalva maneuver for 34 control subjects and 5 patients with autonomic dysfunction*

	Cost	Estimated Parameters						
	J (10^{-3})	B	$\tau_{p,b}$	$\tau_{p,r}$	τ_s	$H_{p,b}$	$H_{p,r}$	H_s
Control (34 subjects)	8 ± 5	0.4 ± 0.3	6.5 ± 5.7	9.6 ± 10.8	14 ± 8	0.5 ± 0.2	0.3 ± 0.2	0.3 ± 0.2
Patient								
1	12	0.04*	0.2*	47*	5	0.4	0.05*	0.1
2	0.5	0.5	17*	41*	36*	0.5	0.4	0.5
3	0.4	0.5	13*	2	16	0.2*	0.07*	0.1
4	0.2	0.5	2	4	13	0.1*	0.09*	0.3
5	0.6	0.09*	23*	4	37*	0.4	0.03*	0.3

Values are means and SDs. Pathologies are listed in Table 1. *Parameter value is outside of 1 SD.

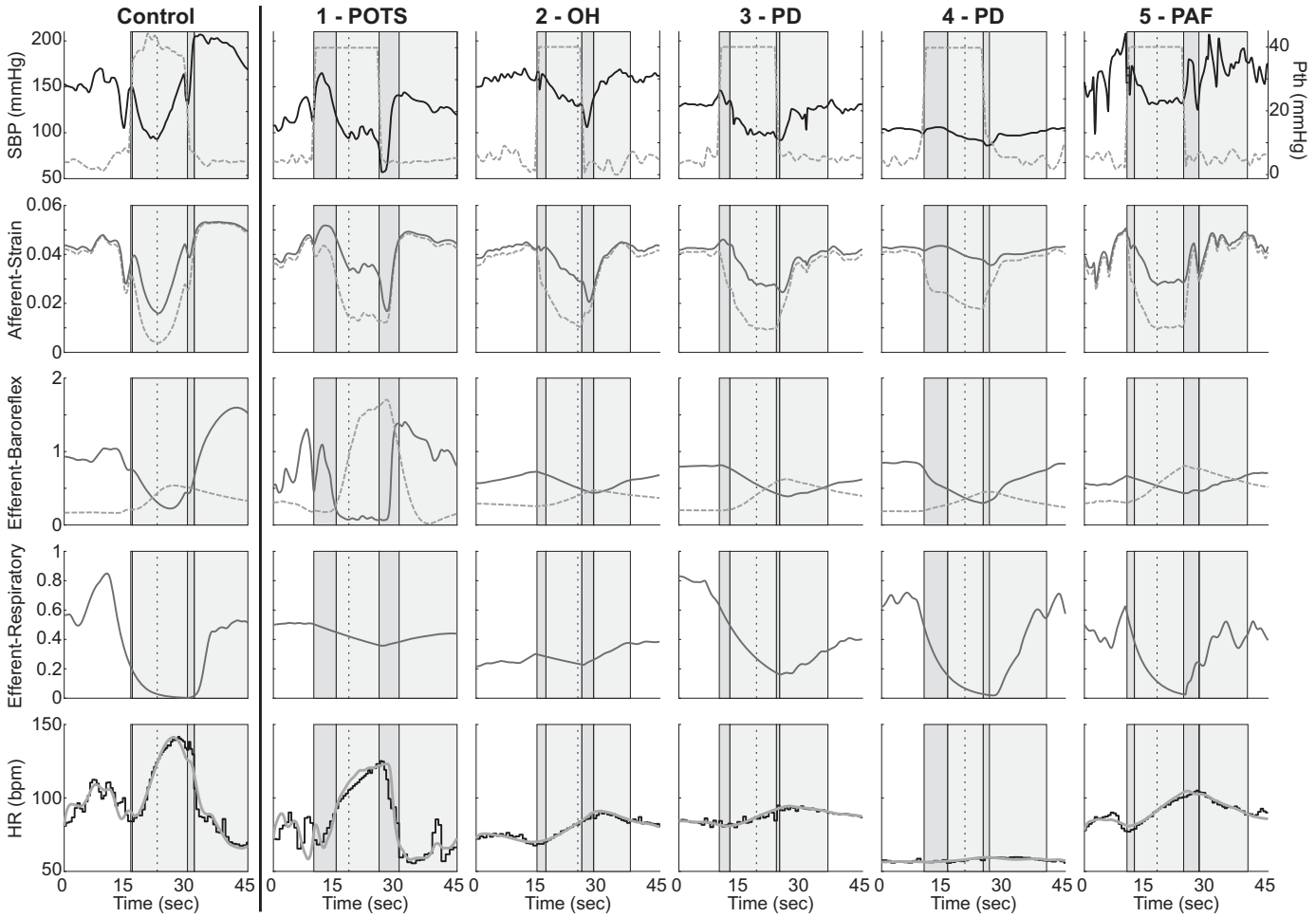

Fig. 8. Data, model fit, and model predictions for *control subject 2* (column 1) and the 5 patients with autonomic dysfunction (columns 2–6). Each column is designated with their particular pathology: postural orthostatic tachycardia syndrome (POTS), orthostatic hypotension (OH), Parkinson's disease (PD), and pure autonomic failure (PAF). Row 1: the inputs with the interpolated systolic blood pressure (SBP, mmHg) plotted from the left *y*-axis and thoracic pressure (P_{th}) plotted from the right *y*-axis. Row 2: predicted baroreceptor strain for the carotid (dark curve) and aortic (light curve) baroreceptors. Row 3: efferent baroreflex response signals for the parasympathetic ($T_{p,b}$, dark curve) and sympathetic (T_s, light curve) outflows. Row 4: efferent respiratory response ($T_{p,r}$). Row 5: model fit (gray) to heart rate data (HR, black). The phases of the Valsalva are designated with alternating gray and light gray boxes. The vertical dashed line delineates between early and late sections of phase II. bpm, beats/min.

vs. female) and age (≤40 yr vs. >40 yr). No statistical differences were detected when accounting for sex, age, or their interactions via a two-way ANOVA (results not included). Thus, the analysis in this study includes all control subjects in one group. The mean value for β agrees with normal baroreceptor sensitivity indices for control subjects in previous studies (31, 48). The mean value with 1 SD for the Valsalva ratio γ also agrees with previous standards (47).

All 5 AD patients were chosen because they exhibit V behavior, which we quantify by a value of $\alpha \ll 1$. Because there was no monotonic increase of SBP back to baseline for *patient 1*, the regression was done over the entire late phase II interval, yielding a negative α value ($\alpha = -0.6$). *Patients 2–4* show no change in SBP in late phase II ($\alpha = 0$). For *Patient 5*, $\alpha = 0.5$ remains below 1 SD of the mean of the control subjects.

The baroreflex sensitivity index β is within normal range for *patients 1*, *3*, and *4*. *Patients 2* and *5* are also within normal range but an order of magnitude smaller ($\beta = 3$) than the mean of the control subjects. This is to be expected for patients with OH, as the change in heart rate is small in relation to the change in SBP.

The Valsalva ratio γ for *patient 1* was greater than the mean of the control subjects, indicating a substantial drop in heart rate from phase III to phase IV. This is to be expected for patients with POTS, as the heart rate has increased significantly during the VM. *Patients 2–5* show $\gamma \approx 1$, indicating abnormal behavior with little to no change in heart rate in the late phases of the VM.

Estimated parameter values. Table 5 displays the mean and SD of the nonlinear least squares cost and estimated parameters of the characteristic VM for all 34 control subjects and 5 AD patients. Again, no statistical differences were detected via a two-way ANOVA accounting for sex and age (results not included). No correlations were found between the clinical ratios and the estimated parameters, which is to be expected because the model is not informed by the clinical ratios. Also, no correlations were found between the calculated parameters in Table 3 and the clinical ratios. This is surprising because we expected the parameters calculated directly from the data to

correlate with the ratios. This could be due to the fact that the clinical ratios reflect transient changes in heart rate and blood pressure, whereas the calculated model parameters are determined from baseline values. The Valsalva ratio in particular is not dependent on baseline values (16). The following paragraphs describe the results from the estimated parameters and the predicted autonomic function of each patient. Table 6 summarizes these results, with arrows signifying either an increase or decrease in function.

For *Patient 1* (POTS), the optimized B value was an order of magnitude smaller than the mean of the control subjects, determining that the aortic baroreceptors contribute the most to the heart rate. The time-scale $\tau_{p,b}$ is an order of magnitude smaller than the mean of the control subjects as well, signifying an overactive baroreflex-mediated parasympathetic outflow. The time-scale τ_s is outside of 1 SD of the mean of the control subjects, indicating increased sympathetic outflow, whereas H_s is within its normal range. The combination of these parameter values implies an increased parasympathetic and sympathetic outflow to the sinoatrial node, which contradicts our hypothesis of diminished parasympathetic and sympathetic activity due to the baroreflex. This is surprising because the V behavior is typically seen in subjects with adrenergic failure. $H_{p,r}$ associated with RSA is approximately zero, signifying that the effect from RSA is negligible for this subject.

Patients 3 and *4* (PD) have parameter values that fall in similar ranges. The parasympathetic parameters, $H_{p,b}$ and $H_{p,r}$, are outside of 1 SD of the mean of the control subjects. This is to be expected because PD tends to drastically affect the parasympathetic nervous system, whereas declines in sympathetic activity occur much later. These subjects also do not coincide with the hypothesis for the V behavior, as only the parasympathetic activity has decreased but the sympathetic activity is within normal range.

The parameter values for *patient 2* (OH) and *patient 5* (PAF) fall in ranges that are indicative of their diagnoses. The B value is an order of magnitude smaller than the mean of the controls, skewing the effect of the baroreceptors on the heart rate to the aortic arch. For *patient 5*, $H_{p,r}$ is lower than 1 SD from the mean, indicating little to no effect of the parasympathetic outflow on heart rate from RSA. Furthermore, τ_s is very large for both ($\tau_s > 30$) relative to the control subjects, indicating a much longer effect of the sympathetic control on heart rate. The combination of these parameter values signifies the dysfunction of both the parasympathetic and sympathetic pathways, which agrees with our hypothesis of the V behavior.

Table 6. *Relative autonomic activity of the 5 patients with autonomic dysfunction exhibiting V behavior compared with the control subject*

	Patient				
	1	2	3	4	5
Baroreflex					
Parasympathetic ($T_{p,b}$)	↑	↓	↓	↓	↓
Sympathetic (T_s)	↑	↓			↓
RSA					
Parasympathetic ($T_{p,r}$)	↓	↓	↓	↓	↓
Agree with V hypothesis?	N	Y	N	N	Y

Blank spaces indicate no change. N, no; RSA, respiratory sinus arrhythmia; Y, yes.

DISCUSSION

This study presents a mathematical model of autonomic nervous control of heart rate before, during, and after the VM through two control mechanisms: RSA and the baroreflex. Because autonomic activity is difficult to measure in vivo and therefore must be analyzed indirectly, modeling sympathetic and parasympathetic signals yields both a quantitative and qualitative assessment of autonomic function. The model, in conjunction with parameter estimation, fits many different kinds of heart rate responses to the VM. The model was effectively validated against 34 control subjects and 5 AD patients, varying widely in age and baseline blood pressure and heart rate values. Several other studies have attempted to model the VM (10, 26, 30, 37, 40, 59). However, our model provides novel facets, such as the inclusion of two input signals, SBP and P_{th}; the delineation between the aortic and carotid baroreceptor centers; the combination of both the ITP and the respiratory signal to determine P_{th}; and the incorporation of a sympathetic delay. The estimated parameters can help explain and differentiate etiologies for AD pathologies not captured by the data and/or clinical ratios alone. In summary, the model (in conjunction with parameter estimation) supplements existing data analysis protocols by providing time series for various neurological pathways and interpretable parameter values for disease classification.

Neural Signals

Because fluctuations in SBP affect parasympathetic outflow, we expect the baroreflex-mediated parasympathetic outflow ($T_{p,b}$) to oscillate with SBP at rest if large changes in SBP occur. During the VM, $T_{p,b}$ accurately depicts parasympathetic withdrawal in phase II; a second, less dramatic parasympathetic withdrawal in phase III; and an overshoot in phase IV, known to occur in control subjects (60, 65). The model captures all of these behaviors for the control subject. The sympathetic outflow should remain relatively constant, or with minor oscillations, at rest. During the VM, the decrease in blood pressure sensed by the HPBs activates the sympathetic nervous system. T_s accurately exhibits a delayed increase in sympathetic activity in phase II and delayed decrease in activity through phases III and IV. The model in conjunction with parameter estimation depicts all of these behaviors. In Fig. 8, $T_{p,b}$ does not fluctuate as dramatically for *patients 2–5* as it does for the control subject, whereas T_s follows a similar trajectory as the control subject. Because the baseline baroreflex-mediated parasympathetic control and baroreflex-mediated sympathetic activation are both known to decline with age and disease (44), the model distinguishes between these differences. However, because our study does not include data for elderly control subjects, we currently cannot differentiate behavior attributed to age or disease.

Inclusion of Aortic and Carotid Bodies

Our study supports the hypothesis that the baroreceptors of the aortic body are necessary to calibrate the model for each subject and effectively capture the VM behavior. Although the values vary widely between subjects, the neural scaling factor

B has a mean value of $0.4 \pm 0.3\ s^{-1}$ for the control subjects, skewing toward the aortic baroreceptors. Kosinski et al. (35) showed that in their model the combined effects of both the carotid and aortic baroreceptor regions is necessary to capture the dynamics of the VM. Our study not only agrees with this finding but emphasizes that the aortic baroreceptors may play a larger role than previously thought in the VM.

Role of Respiratory Sinus Arrhythmia

Figure 9 displays the optimized fit of the model output for the baroreflex-only (dotted curve) and the joint baroreflex-RSA output (solid gray curve). At baseline, the efficacy of the model fit to the heart rate data depends strongly on RSA, which coincides with previous studies (4, 13). By incorporating RSA, these oscillations can be effectively captured. During the VM, the baroreflex-only and joint baroreflex-RSA model outputs fit the data well in late phase II and phases III and IV. However, it should be noted that the discrepancy in phase I and early phase II implies that the baroreflex-only signal cannot simulate the initial heart rate drop caused primarily by the sharp inspiration. This discrepancy also occurs in the heart rate fits to data in Kosinski et al. (35). With the inclusion of RSA, our model can capture this sudden drop in heart rate.

Clinical Ratios

The clinical ratios α, β, and γ were presented in this study. A novel component of our analysis is the definition of the index α, the slope of the increase in blood pressure during late phase II, as a measure of sympathetic nervous activity. In the original study by Korner et al. (34), it was shown that the late phase blood pressure increase depended solely on sympathetic activity. To our knowledge, no other studies have used α to approximate sympathetic function. Although α may be affected by an increased cardiac output in late phase II due to the stabilization of stroke volume at a lower level, we propose that α relates to the effectiveness of the sympathetic response to SBP recovery. The 5 AD patients display little to no ability to recover baseline SBP during late phase II ($\alpha \approx 0$ as shown in Table 4). Increased arteriolar resistance due to sympathetic activation largely contributes to the return of SBP to baseline in late phase II and the overshoot in phase IV (60). Thus, in the absence of sympathetic activation, the peripheral resistance does not increase and as a result SBP does not return to baseline, leading to $\alpha \approx 0$. This analysis supports the use of α as an indicator of sympathetic function.

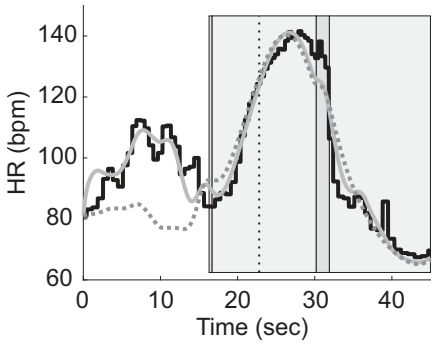

Fig. 9. Respiratory sinus arrhythmia (RSA) effects on the model output for the baroreflex-only (dashed curve) and the joint baroreflex-RSA (solid gray curve). Bpm, beats/min; HR, heart rate.

The values of β, the baroreceptor sensitivity, for *patients 1–4* are within normal range, whereas *patient 5* has a significantly diminished value. Although this index is common (31, 56, 68), interpretation of the ratio is inconclusive. Because this index is a ratio of R-R interval to SBP, various factors can contribute to lower or higher β values. For example, a low β value could be the result of a marginal change in R-R interval from phase III to phase IV, which could be due to a decrease in parasympathetic outflow; a drastic SBP overshoot in phase IV, which could be due to a substantial and sustained increase in sympathetic outflow; or a combination of these. Because of the ambiguous nature of this index, we recommend using the parameters estimated from the proposed model in this study to supplement the explanation of β value. We expound on this notion in the next section.

The Valsalva ratio γ typically associated with vagal function is abnormal when $\gamma \leq 1.1$ (16). We observe what is traditionally determined as 'abnormal' behavior for *patients 2–5*, but γ is very high ($\gamma = 2.3$) for *patient 1* (POTS) and outside of the normal range. Expanding on the definition of abnormal vagal behavior using this index would be very useful clinically. We propose the following delineation for clarity and ease of use:

- $\gamma \leq 1.1$ – abnormal with diminished parasympathetic activity;
- $1.1 < \gamma \leq 2$ – normal range;
- $\gamma > 2$ – abnormal with overactive parasympathetic activity.

Model-based Analysis of Autonomic Dysfunction

As discussed in the previous section, β describes the relationship between changes in R-R interval and SBP but does not explain how those changes arise. Abnormally low or high values of β could be the result of many combinations of parasympathetic and sympathetic dysfunction (68). Furthermore, β could be within the normal range but only describes that the compensatory decrease in heart rate is proportional to the overshoot in SBP. Employing the estimated parameters determined by the methods introduced in this study in comparison to the β value would greatly enhance the interpretative power for these patients. The following discusses each AD patient and compares their clinical ratios to the estimated parameters. Table 6 tabulates the relative parasympathetic and sympathetic responses of the AD patients to the control subjects.

Patient 1 (POTS) has a large increase in heart rate in relation to the SBP overshoot, yielding a β value within normal range and a high γ value. POTS is known to occur without orthostatic hypotension, which is not observed in this patient (43). Although β is normal, this patient clearly has an abnormal VM trace given the V behavior and an increase in heart rate of $\geq$30 beats/min. To characterize the AD contributing to this abnormal behavior, estimated model parameters show overactive baroreflex-mediated parasympathetic (low $\tau_{p,b}$ and normal $H_{p,b}$ values) and sympathetic (low τ_s and normal H_s values) outflows. Therefore, this patient experiences abnormal changes in the activity of both autonomic sectors to the sinoatrial node, contributing to the substantial increase in heart rate.

Patients 2 (OH) and *5* (PAF) maintain a high blood pressure with a sharp decline during the VM without a substantial compensatory heart rate increase (a key factor in their diagnoses) (43). Although the β value for these patients is low, it is still within normal range. The estimated parameters for *patient 2* show that all time-scales have increased substantially (high $\tau_{p,b}$, $\tau_{p,r}$, and τ_s values) with normal heart rate gains ($H_{p,b}$, $H_{p,r}$, and H_s). These indicate that the baroreflex tone has significantly decreased for this patient for both parasympathetic and sympathetic branches. *Patient 5* displays increased $\tau_{p,b}$ and τ_s values, indicating decreased parasympathetic and sympathetic outflow due to the baroreflex, respectively. Furthermore, parameters associated with RSA control are outside of their normal range (high $\tau_{p,r}$ for *patient 2* and low $H_{p,r}$ for *patient 5*), decreasing the effect of $T_{p,r}$ on heart rate, which occurs with age (77). The etiologies for these patients coincide with the hypothesis of the V behavior.

Patients 3 and *4* (PD) both have normal β values while exhibiting almost no change in heart rate in phase IV ($\gamma = 1$) and the V behavior. In regard to the estimated parameter values, both patients show decreased parasympathetic activity. *Patient 3* has a high $\tau_{p,b}$ with low $H_{p,b}$ and $H_{p,r}$, and *patient 4* has low values for heart rate gains $H_{p,b}$ and $H_{p,r}$. Therefore, both PD patients exhibit impaired vagal function for both the baroreflex and RSA, whereas adrenergic function operates normally (τ_s and H_s within normal range). This coincides with PD patients who experience orthostatic hypotension without orthostatic intolerance (54). Hence, the sympathetic outflow for the PD patients may still affect heart rate but not blood pressure. Further investigation is required to substantiate this hypothesis.

The different causes eliciting the V response for these 5 AD patients leads us to conclude that the hypothesis for the V behavior should be expanded. Pattern recognition alone is not sufficient to explain the etiologies for each of the patients; therefore, we can develop subcategories that encompass these explanations. Further investigation into this phenomenon with a larger cohort of subjects exhibiting the V behavior is needed to develop these subcategories.

Model Limitations

ITP data was not recorded for the 5 AD patients. We used *Eq. 5* to obtain an ITP signal, assuming that they maintained an expiratory force of 40 mmHg throughout the breath hold. Moving forward, we suggest the inclusion of time-varying measurements of ITP in all protocols examining the response to the VM. We computed an ECG-derived respiratory signal in lieu of respiratory data, which was not collected for the data analyzed. Because the model uses only the SBP as an input, the Voigt body of *Eq. 9* truly responds to the systolic max arterial wall strain, due to the interpolation of the SBP as a continuous input. In actuality, these Voigt bodies respond to the continuous pulse pressure throughout the cardiac cycle. We do not explicitly model action potential generation but rather a collective neural outflow of the baroreceptors in response to the SBP. The model may benefit from a more explicit neuron model, but this may induce unnecessary complexity by significantly increasing the number of model states and parameters.

An important control mechanism activated in response to the VM is the explicit effect of LPBs, which sense changes in central blood volume in the vena cava and right atrium junctions. The effect of these baroreceptors is difficult to model without either available data for right atrial volume/pressure or the use of a closed-loop cardiovascular model coupled to the presented neurological model. We plan to couple these models in a future study.

The conclusions made in this study are limited by the relatively small group of control subjects. Although these individuals do not exhibit AD in response to the VM, they may experience other conditions not accounted for in this study. Although we used the patients with AD as a mode of comparison to the control subjects, we are limited by the availability of patients that exhibit the V behavior. We would benefit from a larger patient cohort with which to perform a more extensive statistical analysis.

Conclusions

This study proposes a mathematical model of respiratory sinus arrhythmia and the baroreflex in response to the Valsalva maneuver. The model uses SBP and thoracic pressure inputs to delineate the aortic and carotid baroreceptor centers. The model is calibrated to a measured heart rate, simultaneously providing an approximation of respiratory-mediated parasympathetic activity and baroreflex-mediated parasympathetic and sympathetic nervous activity, which cannot be measured noninvasively. Our model performs very well and was validated against 34 control subjects and 5 AD patients. We emphasize the necessity of modeling the two baroreceptor regions to accurately depict the dynamics during the VM, the efferent respiratory pathway to indirectly model effects of low-pressure baroreceptors during the VM, and the delay in sympathetic nervous activity. We have also introduced a new index α, which quantifies the sympathetic gain in late phase II of the VM. Furthermore, our results support that the categorization of the V behavior should be divided into subcategories based on the etiology described by the estimated model parameters. We have found no correlation between the clinical ratios studied and the model outputs, indicating that the model includes quantities not measured by these clinical ratios. In summary, this model in conjunction with parameter estimation can be used to effectively analyze autonomic cardiovascular control.

APPENDIX

Model Development

Initial conditions. The initial conditions were calculated analytically using the SBP, thoracic pressure (P_{th}), and heart rate data values at the initial time point t_0. The model was parameterized to ensure it began in steady-state conditions. The initial conditions for the arterial wall strain for both the carotid and aortic regions are

$$\varepsilon_{w,c}(t_0) = 1 - \sqrt{\frac{1 + e^{-q_w(P_c(t_0) - s_w)}}{A + e^{-q_w(P_c(t_0) - s_w)}}} \tag{A1}$$

and

$$\varepsilon_{w,a}(t_0) = 1 - \sqrt{\frac{1 + e^{-q_w(P_a(t_0) - s_w)}}{A + e^{-q_w(P_a(t_0) - s_w)}}}, \tag{A2}$$

which yields the initial conditions for the baroreceptors

$$\varepsilon_{b,j}(t_0) = K_b \varepsilon_{w,j}(t_0), \tag{A3}$$

where $j = c$ or a for carotid and aortic, respectively. The initial neural integration is

$$n(t_0) = B\big(\varepsilon_{w,c}(t_0) - \varepsilon_{b,c}(t_0)\big) + \big(1 - B\big)\big(\varepsilon_{w,a}(t_0) - \varepsilon_{b,a}(t_0)\big). \tag{A4}$$

The initial condition for the baroreflex-mediated parasympathetic outflow is

$$T_{p,b}(t_0) = K_{p,b} G_{p,b}(t_0) = \frac{K_{p,b}}{1 + e^{-q_{p,b}(n(t_0) - s_{p,b})}}, \tag{A5}$$

and the history for the delayed sympathetic outflow is set constant to the initial condition

$$T_s(t_0) = K_s G_s(t_0) = \frac{K_s}{1 + e^{q_s(n(t_0) - s_s)}}, \tag{A6}$$

for simplicity. The initial condition for the respiratory-mediated parasympathetic outflow is

$$T_{p,r}(t_0) = K_{p,r} G_{p,r}(t_0) = \frac{K_{p,r}}{1 + e^{q_{p,r}(P_{th}(t_0) - s_{p,r})}}. \tag{A7}$$

The initial condition for the heart rate ordinary differential equation is

$$H(t_0) = H_{data}(t_0). \tag{A8}$$

Nominal Parameter Values

Some parameters are calculated a priori to calibrate the model to each individual subject. The half-saturation values of the sigmoidal relationships for the arterial wall strain, s_w, and the efferent respiratory pathway, $s_{p,r}$, can be interpreted as the baseline SBP and baseline P_{th}, respectively, calculated as the average value over 15 s of rest, i.e.,

$$s_w = \bar{P} \text{ and } s_{p,r} = \bar{P}_{th}. \tag{A9}$$

The half-saturation values of the baroreflex-mediated parasympathetic and sympathetic sigmoids, $s_{p,b}$ and s_s, are calculated assuming that the parasympathetic activity contributed 80% of the baroreflex control of the heart rate at rest and the sympathetic activity contributed 20% (11, 62). We chose the 80:20 ratio so as to account for the tremendous variation in the subjects' ages and the variegated data itself, especially because sympathetic nervous system activity at rest generally increases with age (27). The bars in the following calculations indicate average values calculated from the SBP, P_{th}, and heart rate data ($\bar{P}$, $\bar{P}_{th}$, $\bar{H}$). The half-saturation values are as follows:

$$\bar{P}_c = \bar{P},$$

$$\bar{P}_a = \bar{P} - \bar{P}_{th},$$

$$\bar{\varepsilon}_{w,j} = \sqrt{\frac{1 + e^{-q_w(\bar{P}_j - s_w)}}{A + e^{-q_w(\bar{P}_j - s_w)}}},$$

$$\bar{\varepsilon}_{b,j} = K_b \bar{\varepsilon}_{w,j},\ \bar{n} = B\big(\bar{\varepsilon}_{w,c} - \bar{\varepsilon}_{b,c}\big) + \big(1 - B\big)\big(\bar{\varepsilon}_{w,a} - \bar{\varepsilon}_{b,a}\big),$$

$$s_{p,b} = \bar{n} + \frac{1}{q_{p,b}} \ln\left(\frac{K_{p,b}}{\bar{T}_{p,b}} - 1\right) \text{ and } s_s = \bar{n} - \frac{1}{q_s} \ln\left(\frac{K_s}{\bar{T}_s} - 1\right), \tag{A10}$$

where $\bar{T}_{p,b} = 0.8$, $\bar{T}_s = 0.2$, and $j = c$ or a.

We calculate the intrinsic heart rate, H_I, as a function of age,

$$H_I = 118 - 0.57\text{age} \tag{A11}$$

(29). We calculate the sympathetic coefficient for heart rate, H_s, by determining the maximal heart rate possible based on age using the equation from Tanaka et al. (69),

$$H_M = 208 - 0.7\text{age}. \tag{A12}$$

To attain the maximal heart rate, we assume sympathetic activity should be at its highest value and parasympathetic activity at its lowest value, i.e., $G_{p,b} = G_{p,r} = 0$ and $G_s = 1$. Then,

$$H_M = H_I\big(1 + H_s K_s\big) \Rightarrow H_s = \frac{1}{K_s}\left(\frac{H_M}{H_I} - 1\right). \tag{A13}$$

The nominal value for the respiratory-mediated parasympathetic scaling factor for heart rate, $H_{p,r}$, is calculated by finding the largest value in the heart rate data due to respiration during rest, $H_{R,M}$, and the lowest value, $H_{R,m}$, i.e.,

$$H_{p,r} = \frac{H_{R,M} - H_{R,m}}{H_I} \frac{1}{\bar{T}_{p,r}}, \tag{A14}$$

where $\bar{T}_{p,r}$ is the steady-state respiratory-mediated parasympathetic outflow set at 0.5 s^{-1}. The baroreflex-mediated parasympathetic outflow parameter is reverse-engineered from the resting heart rate equation using the baseline heart rate, $\bar{H}$, which yields

$$H_{p,b} = \frac{1 - \dfrac{\bar{H}}{H_I} + H_{p,r}\bar{T}_{p,r} + H_s\bar{T}_s}{\bar{T}_{p,b}}. \tag{A15}$$

Model Analysis

Sensitivity analysis. We conducted a local sensitivity analysis, as discussed in the *Model Analysis* section, by computing the sensitivity matrix $\boldsymbol{S}$ (*Eq. 20*) and ranking the parameter indices s (*Eq. 21*). We did not include times extricated from data, t_s and t_e, in the sensitivity analysis. Naturally, the model is very sensitive to changes in these parameters, but we set them constant to ensure patient specificity. Thus, we only consider 24 parameters in the sensitivity analysis (Fig. 7). All of the parameters were above the sensitivity threshold of 10^{-3}. We determined $s_{p,b}$, s_w, H_I, and A were the most sensitive parameters. Since these parameters are highly sensitive, small fluctuations cause large changes in the model output. Changes in the least sensitive parameters, $q_{p,r}$, and τ_b, show a negligible change in model output.

Correlation analysis and subset selection. We performed a local correlation analysis to determine possible pairwise correlations between sensitive parameters. Following Olufsen and Ottesen (49), we compute the correlation matrix $\boldsymbol{c}$ (*Eq. 22*), which is symmetric where $|c_{i,i}| = 1$ and $|c_{i,j}| \leq 1$. We analyzed pairwise correlations between only a subset of parameters. The sigmoid half-saturation values, s_w, $s_{p,r}$, $s_{p,b}$, and s_s, are calculated as shown above. The half-saturation values are difficult to optimize, as the optimized result can force the model to produce a linear relation where nonlinearity occurs physiologically. Estimating the sigmoid steepness parameters, q_w, $q_{p,r}$, $q_{p,b}$, and q_s, poses similar challenges by producing neural signals that are not physiological. Thus, we left these parameters fixed. As with the sensitivity analysis, we excluded the time parameters from the correlation analysis.

The subset of parameters for consideration for the structured correlation analysis includes

$$\hat{\theta} = \big[A, B, K_b, K_{p,b}, K_{p,r}, K_s, \tau_b, \tau_{p,b}, \tau_{p,r}, \tau_s, \tau_H, H_I, H_{p,b}, H_{p,r}, H_s, D_s\big]^T. \tag{A16}$$

This method works by computing a correlation matrix $\boldsymbol{c}$ (*Eq. 22*) and identifying parameters with a correlation coefficient $|c_{i,j}| \geq 0.95$. We

fix the least influential parameter (determined by the local sensitivity analysis) at its nominal value and repeat the analysis until we obtain a subset free of pairwise correlations. This analysis yields

$$\tilde{\theta} = \left[B, \tau_{p,b}, \tau_{p,r}, \tau_s, H_{p,b}, H_{p,r}, H_s\right]^T, \quad (A17)$$

in which the parameters are above the sensitivity threshold and are not pairwise correlated. Furthermore, we confirmed this subset was correlation-free with a global sensitivity analysis using DRAM. DRAM combines the delayed rejection and adaptive metropolis algorithms to improve the efficiency of the Metropolis-Hastings algorithm (22). Although correlation analysis is far less computationally expensive than DRAM, it only calculates a first-order linearization of the parameter interactions and therefore does not take into account the higher order parameter interactions. In this regard, DRAM is much more suited for capturing the nuances of nonlinear parameter interactions and ensures our subset was identifiable. Moreover, we conducted a cross-validation of the parameters by altering the nominal parameter values and reoptimizing. We then analyzed 10 reoptimization iterations and found that the coefficient of variation (σ/μ for σ the SD and μ the mean) was $\sigma/\mu < 0.15$ for all parameters in this set.

ACKNOWLEDGMENTS

We thank Dr. D.A. Beard, Molecular and Integrative Physiology, University of Michigan for fruitful discussions on the integration of afferent firing from aortic and carotid baroreceptors.

GRANTS

This study was supported in part by the National Science Foundation under the Division of Mathematical Sciences Awards 1246991 and 1557761, as well as the Virtual Physiology Rat National Center for Systems Biology Project funded by the National Institutes of Health/National Institute of General Medical Sciences P50-GM094503.

DISCLOSURES

No conflicts of interest, financial or otherwise, are declared by the authors.

AUTHOR CONTRIBUTIONS

E.B.R., A.B., L.S.B., J.M., and M.S.O. conceived and designed research; A.B. and L.S.B. performed experiments; E.B.R. and M.S.O. analyzed data; E.B.R., J.M., and M.S.O. interpreted results of experiments; E.B.R. and M.S.O. prepared figures; E.B.R. and M.S.O. drafted manuscript; E.B.R., J.M., and M.S.O. edited and revised manuscript; E.B.R., A.B., L.S.B., J.M., and M.S.O. approved final version of manuscript.

REFERENCES

1. **Airaksinen KE, Hartikainen JE, Niemelä MJ, Huikuri HV, Mussalo HM, Tahvanainen KU.** Valsalva manoeuvre in the assessment of baroreflex sensitivity in patients with coronary artery disease. *Eur Heart J* 14: 1519–1523, 1993. doi:10.1093/eurheartj/14.11.1519.
2. **Arndt JO, Morgenstern J, Samodelov L.** The physiologically relevant information regarding systemic blood pressure encoded in the carotid sinus baroreceptor discharge pattern. *J Physiol* 268: 775–791, 1977. doi:10.1113/jphysiol.1977.sp011881.
3. **Bai J, Lu H, Zhang J, Zhao B, Zhou X.** Optimization and mechanism of step-leap respiration exercise in treating of cor pulmonale. *Comput Biol Med* 28: 289–307, 1998. doi:10.1016/S0010-4825(98)00009-2.
4. **Ben-Tal A, Shamailov SS, Paton JFR.** Central regulation of heart rate and the appearance of respiratory sinus arrhythmia: new insights from mathematical modeling. *Math Biosci* 255: 71–82, 2014. doi:10.1016/j.mbs.2014.06.015.
5. **Berger RD, Saul JP, Cohen RJ.** Transfer function analysis of autonoic regulation. I. Canine atrial rate response. *Am J Physiol Heart Circ Physiol* 256: H142–H152, 1989. doi:10.1152/ajpheart.1989.256.1.H142.
6. **Bevan JA, Verity MA.** Postganglionic sympathetic delay in vascular smooth muscle. *J Pharmacol Exp Ther* 152: 221–230, 1966.
7. **Boron WF, Boulpaep EL.** *Medical Physiology: A Cellular and Molecular Approach*. (2nd ed.). Philadelphia, PA: Elsevier, 2009.
8. **Braunwald E, Oldham HN Jr, Ross J Jr, Linhart JW, Mason DT, Fort L III.** The circulatory response of patients with idiopathic hypertrophic subaortic stenosis to nitroglycerin and to the Valsalva maneuver. *Circulation* 29: 422–431, 1964. doi:10.1161/01.CIR.29.3.422.
9. **Brown TP.** Pure autonomic failure. *Pract Neurol* 17: 341–348, 2017. doi:10.1136/practneurol-2016-001559.
10. **Bugenhagen SM, Cowley AW Jr, Beard DA.** Identifying physiological origins of baroreflex dysfunction in salt-sensitive hypertension in the Dahl SS rat. *Physiol Genomics* 42: 23–41, 2010. doi:10.1152/physiolgenomics.00027.2010.
11. **Craft N, Schwartz JB.** Effects of age on intrinsic heart rate, heart rate variability, and AV conduction in healthy humans. *Am J Physiol Heart Circ Physiol* 268: H1441–H1452, 1995. doi:10.1152/ajpheart.1995.268.4.H1441.
12. **De Lazzari C, Darowski M, Ferrari G, Pisanelli DM, Tosti G.** Modelling in the study of interaction of Hemopump device and artificial ventilation. *Comput Biol Med* 36: 1235–1251, 2006. doi:10.1016/j.compbiomed.2005.08.001.
13. **deBoer RW, Karemaker JM, Strackee J.** Hemodynamic fluctuations and baroreflex sensitivity in humans: a beat-to-beat model. *Am J Physiol Heart Circ Physiol* 253: H680–H689, 1987. doi:10.1152/ajpheart.1987.253.3.H680.
14. **Ellwein LM, Tran HT, Zapata C, Novak V, Olufsen MS.** Sensitivity analysis and model assessment: mathematical models for arterial blood flow and blood pressure. *Cardiovasc Eng* 8: 94–108, 2008. doi:10.1007/s10558-007-9047-3.
15. **Eslami M.** *Theory of Sensitivity in Dynamic Systems: An Introduction*. Berlin/Heiderlberg, Germany: Springer-Verlag, 1994.
16. **Freeman R, Chapleau MW.** Testing the autonomic nervous system. *Handb Clin Neurol* 115: 115–136, 2013. doi:10.1016/B978-0-444-52902-2.00007-2.
17. **Fritsch FN, Carlson RE.** Monotone piecewise cubic interpolation. *SIAM J Numer Anal* 17: 238–246, 1980. doi:10.1137/0717021.
18. **Fung YC.** *Biomechanics: Circulation*. New York: Springer-Verlag, 1996.
19. **García-Lledó A, Moya JL, Balaguer J.** Prognostic value of Valsalva maneuver-induced change in Doppler-detected ventricular filling in patients with systolic dysfunction [in Spanish]. *Rev Esp Cardiol* 58: 1029–1036, 2005.
20. **Guglielmi N, Hairer E.** Implementing Radau IIA methods for stiff delay differential equations. *Computing* 67: 1–12, 2001. doi:10.1007/s006070170013.
21. **Franz GN.** Nonlinear rate sensitivity of the carotid sinus reflex as a consequence of static and dynamic nonlinearities in baroreceptor behavior. *Ann N Y Acad Sci* 156: 811–824, 1969. doi:10.1111/j.1749-6632.1969.tb14016.x.
22. **Haario H, Laine M, Mira A, Saksman E.** DRAM: Efficient adaptive MCMC. *Stat Comput* 16: 339–354, 2006. doi:10.1007/s11222-006-9438-0.
23. **Hall JE.** *Guyton and Hall Textbook of Medical Physiology*. Philadelphia, PA: Elsevier, Inc, 2016.
24. **Hamilton WF, WoodBury RA, Harper HT Jr.** Arterial, cerebrospinal, and venous pressures in man during cough and strain. *Am Heart J* 141: 42–50, 1944. doi:10.1152/ajplegacy.1944.141.1.42.
25. **Helfenbein E, Firoozabadi R, Chien S, Carlson E, Babaeizadeh S.** Development of three methods for extracting respiration from the surface ECG: a review. *J Electrocardiol* 47: 819–825, 2014. doi:10.1016/j.jelectrocard.2014.07.020.
26. **Hemalatha K, Manivannan M.** Valsalva maneuver for the analysis of interaction hemodynamic model study. *2010 International Conference on Recent Trends in Information, Telecommunication, and Computing*. 2010: 28–32, 2010. doi:10.1109/ITC.2010.54.
27. **Hotta H, Uchida S.** Aging of the autonomic nervous system and possible improvements in autonomic activity using somatic afferent stimulation. *Geriatr Gerontol Int* 10, *Suppl* 1: S127–S136, 2010. doi:10.1111/j.1447-0594.2010.00592.x.
28. **Jennings GL, Gelman JS, Stockigt JR, Korner PI.** Accentuated hypotensive effect of sodium nitroprusside in man after captopril. *Clin Sci (Lond)* 61: 521–526, 1981. doi:10.1042/cs0610521.
29. **Jose AD, Collison D.** The normal range and determinants of the intrinsic heart rate in man. *Cardiovasc Res* 4: 160–167, 1970. doi:10.1093/cvr/4.2.160.
30. **Kana M, Holcik J.** Mathematical model-based markers of autonomic nervous activity during the Valsalva Maneuver and comparison to heart rate variability. *Biomed Signal Process Control* 6: 251–260, 2011. doi:10.1016/j.bspc.2011.05.001.

31. **Kautzner J, Hartikainen JE, Camm AJ, Malik M.** Arterial baroreflex sensitivity assessed from phase IV of the Valsalva maneuver. *Am J Cardiol* 78: 575–579, 1996. doi:10.1016/S0002-9149(96)00370-0.
32. **Kelley CT.** *Iterative Methods for Optimization*. Philadelphia, PA: Society for Industrial and Applied Mathematics, 1996.
33. **Kobayashi H.** Normalization of respiratory sinus arrhythmia by factoring in tidal volume. *Appl Human Sci* 17: 207–213, 1998. doi:10.2114/jpa.17.207.
34. **Korner PI, Tonkin AM, Uther JB.** Reflex and mechanical circulatory effects of graded Valsalva maneuvers in normal man. *J Appl Physiol* 40: 434–440, 1976. doi:10.1152/jappl.1976.40.3.434.
35. **Kosinski SA, Carlson BE, Hummel SL, Brook RD, Beard DA.** Computational model-based assessment of baroreflex function from response to Valsalva maneuver. *J Appl Physiol (1985)* 125: 1944–1967, 2018. doi:10.1152/japplphysiol.00095.2018.
36. **Le Rolle V, Beuchee A, Praud JP, Samson N, Pladys P, Hernández AI.** Recursive identification of an arterial baroreflex model for the evaluation of cardiovascular autonomic modulation. *Comput Biol Med* 66: 287–294, 2015. doi:10.1016/j.compbiomed.2015.09.013.
37. **Le Rolle V, Hernandez AI, Richard PY, Carrault G.** An autonomic nervous system model applied to the analysis of orthostatic tyests. *Model Simul Eng* 2008: 1–15, 2008. doi:10.1155/2008/427926.
38. **Le Rolle V, Ojeda D, Beuchée A, Praud JP, Pladys P, Hernández AI.** A model-based approach for the evaluation of vagal and sympathetic activities in a newborn lamb. *Conf Proc IEEE Eng Med Biol Soc* 2013: 3881–3884, 2013. doi:10.1109/EMBC.2013.6610392.
39. **Lin J, Ngwompo RF, Tilley DG.** Development of a cardiopulmonary mathematical model incorporating a baro-chemoreceptor reflex control system. *Proc Inst Mech Eng H* 226: 787–803, 2012. doi:10.1177/0954411912451823.
40. **Lu K, Clark JW Jr, Ghorbel FH, Ware DL, Bidani A.** A human cardiopulmonary system model applied to the analysis of the Valsalva maneuver. *Am J Physiol Heart Circ Physiol* 281: H2661–H2679, 2001. doi:10.1152/ajpheart.2001.281.6.H2661.
41. **Mader G, Olufsen M, Mahdi A.** Modeling cerebral blood flow velocity during orthostatic stress. *Ann Biomed Eng* 43: 1748–1758, 2015. doi:10.1007/s10439-014-1220-4.
42. **Mahdi A, Sturdy J, Ottesen JT, Olufsen MS.** Modeling the afferent dynamics of the baroreflex control system. *PLOS Comput Biol* 9: e1003384, 2013. doi:10.1371/journal.pcbi.1003384.
43. **Mathias CJ.** Autonomic diseases: clinical features and laboratory evaluation. *J Neurol Neurosurg Psychiatry* 74, *Suppl* 3: iii31–iii41, 2003. doi:10.1136/jnnp.74.suppl_3.iii31.
44. **Monahan KD.** Effect of aging on baroreflex function in humans. *Am J Physiol Regul Integr Comp Physiol* 293: R3–R12, 2007. doi:10.1152/ajpregu.00031.2007.
45. **Nichols WW, Edwards DG.** Arterial elastance and wave reflection augmentation of systolic blood pressure: deleterious effects and implications for therapy. *J Cardiovasc Pharmacol Ther* 6: 5–21, 2001. doi:10.1177/107424840100600102.
46. **Novak P.** Assessment of sympathetic index from the Valsalva maneuver. *Neurology* 76: 2010–2016, 2011. doi:10.1212/WNL.0b013e31821e5563.
47. **Novak P.** Quantitative autonomic testing. *J Vis Exp* 2011: e2502, 2011. doi:10.3791/2502.
48. **O'Leary DD, Kimmerly DS, Cechetto AD, Shoemaker JK.** Differential effect of head-up tilt on cardiovagal and sympathetic baroreflex sensitivity in humans. *Exp Physiol* 88: 769–774, 2003. doi:10.1113/eph8802632.
49. **Olufsen MS, Ottesen JT.** A practical approach to parameter estimation applied to model predicting heart rate regulation. *J Math Biol* 67: 39–68, 2013. doi:10.1007/s00285-012-0535-8.
50. **Olufsen MS, Tran HT, Ottesen JT, Lipsitz LA, Novak V; Research Experiences for Undergraduates Program.** Modeling baroreflex regulation of heart rate during orthostatic stress. *Am J Physiol Regul Integr Comp Physiol* 291: R1355–R1368, 2006. doi:10.1152/ajpregu.00205.2006.

50a. **Ottesen JT.** Modeling the dynamical baroreflex feedback control. *Math Comput Model* 31: 167–173, 2000. doi:10.1016/S0895-7177(00)00035-2.

51. **Ottesen JT, Mehlsen J, Olufsen MS.** Structural correlation method for model reduction and practical estimation of patient specific parameters illustrated on heart rate regulation. *Math Biosci* 257: 50–59, 2014. doi:10.1016/j.mbs.2014.07.003.
52. **Palamarchuk I, Baker J, Kimpinski K.** Non-invasive measurement of adrenergic baroreflex during Valsalva maneuver reveals three distinct patterns in healthy subjects. *Clin Neurophysiol* 127: 858–863, 2016. doi:10.1016/j.clinph.2015.04.057.
53. **Palamarchuk IS, Baker J, Kimpinski K.** The utility of Valsalva maneuver in the diagnoses of orthostatic disorders. *Am J Physiol Regul Integr Comp Physiol* 310: R243–R252, 2016. doi:10.1152/ajpregu.00290.2015.
54. **Palma J-A, Kaufmann H.** Autonomic disorders predicting Parkinson's disease. *Parkinsonism Relat Disord* 20, *Suppl* 1: S94–S98, 2014. doi:10.1016/S1353-8020(13)70024-5.
55. **Parashar R, Amir M, Pakhare A, Rathi P, Chaudhary L.** Age related changes in autonomic functions. *J Clin Diagn Res* 10: CC11–CC15, 2016. doi:10.7860/JCDR/2016/16889.7497.
56. **Piccirillo G, Cacciafesta M, Viola E, Santagada E, Nocco M, Lionetti M, Bucca C, Moisè A, Tarantini S, Marigliano V.** Influence of aging on cardiac baroreflex sensitivity determined non-invasively by power spectral analysis. *Clin Sci (Lond)* 100: 267–274, 2001. doi:10.1042/CS20000222.
57. **Pomeranz B, Macaulay RJ, Caudill MA, Kutz I, Adam D, Gordon D, Kilborn KM, Barger AC, Shannon DC, Cohen RJ, Benson H.** Assessment of autonomic function in humans by heart rate spectral analysis. *Am J Physiol Heart Circ Physiol* 248: H151–H153, 1985. doi:10.1152/ajpheart.1985.248.1.H151.
58. **Pope SR, Ellwein LM, Zapata CL, Novak V, Kelley CT, Olufsen MS.** Estimation and identification of parameters in a lumped cerebrovascular model. *Math Biosci Eng* 6: 93–115, 2009. doi:10.3934/mbe.2009.6.93.
59. **Pstras L, Thomaseth K, Waniewski J, Balzani I, Bellavere F.** Mathematical modelling of cardiovascular response to the Valsalva manoeuvre. *Math Med Biol* 261–292, 2016. doi:10.1093/imammb/dqw008.
60. **Pstras L, Thomaseth K, Waniewski J, Balzani I, Bellavere F.** The Valsalva manoeuvre: physiology and clinical examples. *Acta Physiol (Oxf)* 217: 103–119, 2016. doi:10.1111/apha.12639.
61. **Ramya K, Rajkumar K.** Respiration rate diagnosis using single lead ECG in real time. *Global J Med Res* 13: 7–12, 2013.
62. **Robinson BF, Epstein SE, Beiser GD, Braunwald E.** Control of heart rate by the autonomic nervous system. Studies in man on the interrelation between baroreceptor mechanisms and exercise. *Circ Res* 19: 400–411, 1966. doi:10.1161/01.RES.19.2.400.
63. **Schrezenmaier C, Singer W, Swift NM, Sletten D, Tanabe J, Low PA.** Adrenergic and vagal baroreflex sensitivity in autonomic failure. *Arch Neurol* 64: 381–386, 2007. doi:10.1001/archneur.64.3.381.
64. **Shi Y, Lawford P, Hose R.** Review of zero-D and 1-D models of blood flow in the cardiovascular system. *Biomed Eng Online* 10: 33, 2011. doi:10.1186/1475-925X-10-33.
65. **Smith ML, Beightol LA, Fritsch-Yelle JM, Ellenbogen KA, Porter TR, Eckberg DL.** Valsalva's maneuver revisited: a quantitative method yielding insights into human autonomic control. *Am J Physiol Heart Circ Physiol* 271: H1240–H1249, 1996. doi:10.1152/ajpheart.1996.271.3.H1240.
66. **Smith RC.** *Uncertainty Quantification: Theory, Implementation, and Applications*. Philadelphia, PA: Society for Industrial and Applied Mathematics, 2014.
67. **Spickler JW, Kezdi P, Geller E.** Transfer characteristics of the carotid sinus pressure control system. In: *Baroreceptors and Hypertension*, edited by Kezdi P. Oxford, UK: Pergamon Press, 1967, p. 31–40.
68. **Swenne CA.** Baroreflex sensitivity: mechanisms and measurement. *Neth Heart J* 21: 58–60, 2013. doi:10.1007/s12471-012-0346-y.
69. **Tanaka H, Monahan KD, Seals DR.** Age-predicted maximal heart rate revisited. *J Am Coll Cardiol* 37: 153–156, 2001. doi:10.1016/S0735-1097(00)01054-8.
70. **Thomas RJ, Mietus JE, Peng C-K, Goldberger AL.** An electrocardiogram-based technique to assess cardiopulmonary coupling during sleep. *Sleep* 28: 1151–1161, 2005. doi:10.1093/sleep/28.9.1151.
71. **Valdez-Jasso D.** *Modeling and Identification of Vascular Biomechanical Properties in Large Arteries* (Dissertation). North Carolina: North Carolina State University, 2010.
72. **Valdez-Jasso D, Banks HT, Haider MA, Bia D, Zocalo Y, Armentano RL, Olufsen MS.** Viscoelastic models for passive arterial wall dynamics. *Adv Appl Math Mech* 1: 151–165, 2009.
73. **Wang Z, Yuan LJ, Cao TS, Yang Y, Duan YY, Xing CY.** Simultaneous beat-by-beat investigation of the effects of the Valsalva maneuver on left and right ventricular filling and the possible mechanism. *PLoS One* 8: e53917, 2013. doi:10.1371/journal.pone.0053917.
74. **Wesseling KH, Settels JJ.** Circulatory model of baro- and cardiopulmonary reflexes. In: *Blood Pressure and Heart Rate Variability*. Amsterdam, The Netherlands: IOS Press, 1993.

75. **Widjaja D, Taelman J, Vandeput S, Braeken MA, Otte RO, Van den Bergh BR, Van Huffel S.** ECG-derived respiration: comparison and new measures for respiratory variability. *Comput Cardiol* 37: 149–152, 2010.
76. **Williams ND, Wind-Willassen Ø, Wright AA, Mehlsen J, Ottesen JT, Olufsen MS; REU Program.** Patient-specific modelling of head-up tilt. *Math Med Biol* 31: 365–392, 2014. doi:10.1093/imammb/dqt004.
77. **Yasuma F, Hayano J.** Respiratory sinus arrhythmia: why does the heartbeat synchronize with respiratory rhythm? *Chest* 125: 683–690, 2004. doi:10.1378/chest.125.2.683.
78. **Zygmunt A, Stanczyk J.** Methods of evaluation of autonomic nervous system function. *Arch Med Sci* 6: 11–18, 2010. doi:10.5114/aoms.2010.13500.